UNIVERSIDAD NACIONAL AUTÓNOMA DE MÉXICO

Programa de Posgrado en Astrofísica

Instituto de Radioastronomía y Astrofísica

Recombination Lines and Molecular Gas from Hypercompact HII regions in W51 A

TESIS
QUE PARA OPTAR POR EL GRADO DE:
MAESTRO EN CIENCIAS (ASTROFÍSICA)

Presenta:
Rudy A. Rivera Soto

Tutor:
Dr. Roberto Galván Madrid
Instituto de Radioastronomía y Astrofísica

Morelia, Michoacán. Julio/2020

Dedicatoria ...

Le dedico la obra expuesta en este documento a mi madre, Nayda y a mi padre, Rudy, quienes inculcaron en mi los valores de la honestidad, responsabilidad y perseverancia, fundamentales en mi desarrollo académico, pero además el amor, la paciencia y la empatía, escenciales para mi desarrollo personal. Por el amor y las enseñanzas que me han hecho mejor persona les estaré infinítamente agradecido, y los amaré por siempre.

Resumen de Tesis (*Thesis Summary*)

Los sitios de formación estelar en las galaxias del Universo están dominados por gas molecular. Las estrellas masivas se forman en las zonas más densas dentro de las Nubes Moleculares Gigantes (*GMC's*, 'Giant Molecular Clouds', por sus siglas en inglés). Las *GMC's* contienen subestructuras autogravitantes en su interior conocidas como grumos ('clumps', en inglés) (escalas de $\sim$ pc) y núcleos ('cores', en inglés) (escalas de ~ 0.01 pc) en las que el material acretante da lugar a la formación de cúmulos y pequeños sistemas estelares, respectivamente. Cuando las estrellas alcanzan la Secuencia Principal de Edad Cero (*ZAMS*, 'Zero-Age Main Sequence', en inglés) la radiación ultravioleta emitida por sus atmósferas es suficiente para ionizar sus propios flujos de acreción y demás gas circundante, generando así una región HII.

Las regiones HII son inicialmente pequeñas (tamaño < 0.01 pc), densas ($n_e > 10^4$ cm^{-3}) y están envueltas en polvo y gas molecular. Se cree que las llamadas regiones HII hipercompactas (HC), de tamaños $< 10^{-2}$ pc, y ultracompactas (UC), de tamaños entre 10^{-2} a 10^{-1} pc, son etapas sucesivas en la evolución temprana de la ionización poco después de que una estrella masiva llega a la *ZAMS*. Sus tamaños lo determinan la condición de equilibrio de ionización, o el balance entre la tasa de fotoionización y la tasa de recombinaciones radiativas de los electrones libres (térmicos). Algunos tipos de emisión observable de estas regiones HII embebidas incluyen emisión de continuo libre-libre y de polvo, así como de líneas moleculares y líneas de recombinación de hidrógeno (*RLs*, 'Recombination Lines', en inglés). Las HC HII son típicamente tenues y muy embebidas. Por lo tanto, nuestro conocimiento de ellas se ha basado típicamente en sus observables del continuo centimétrico (el cual contribuye significativamente entre $0.3 < \lambda < 30$ cm).

En este trabajo utilizamos observaciones con resolución de sub-arcosegundo hechas por los interferómetros VLA ('Very Large Array', en inglés) y ALMA ('Atacama Large

Millimeter Array', en inglés) sobre el contenido de gas ionizado y gas molecular en la nube molecular W51 A de la Vía Láctea. El objetivo es caracterizar en detalle su población de fuentes radio-continuo dentro del esquema de clasificación de compacto/UC/HC mediante determinaciones de sus tamaños y densidades electrónicas, y además caracterizar la cinemática del gas ionizado y molecular de estos objetos. Analizamos estos objetos a través de su emisión de continuo a 2 cm (13.4 GHz), dos líneas de recombinación (H77α a 14.12 GHz y H30α a 231.90 GHz) y tres líneas moleculares (H$_2$CO($3_{0,3} - 2_{0,2}$) a 218.22 GHz, H$_2$CO($3_{2,1} - 2_{2,0}$) a 218.76 GHz y SO($6_5 - 5_4$) a 219.95 GHz).

A partir de la emisión de 2 cm derivamos diámetros D para 10/20 objetos en rangos de $D \sim 10^{-3}$ a 10^{-2} pc, lo cual los coloca en el régimen de las regiones HC HIIs. En adición derivamos densidades electrónicas n_e en rangos de $n_e \sim 10^4$ a 10^5 cm $^{-3}$, menores que los valores típicamente asociados a las HC. Además, determinamos la tasa de fotones ionizantes del continuo Lyman requeridos para producir la emisión observada, y se encontró que en su mayoría parecen corresponder a estrellas de tipo espectral B temprana.

Se detectaron 8/20 objetos con H77α y 8/20 objetos con H30α. A partir de las RL derivamos densidades electrónicas e inferimos la cinemática del gas ionizado para los 7/20 objetos que poseen detecciones en ambas líneas. El ancho de las RL tiene contribuciones de componentes termales y de presión (colisionales), encima del ancho dinámico. El ensanchamiento por presión es significativo en RLs centimétricos como H77α y despreciable en RLs milimétricos como H30α, debido a la fuerte dependencia con el número cuántico principal. Aprovechamos este hecho para aislar los diferentes componentes de ensanchamiento de línea y derivar densidades electrónicas. Los rangos de estas mediciones son consistentes con los derivados a partir del continuo ($n_e \sim 10^4$ a 10^5 cm $^{-3}$). En adición, dado que el H30α traza densidades más altas que el H77α (suponiendo un perfil de densidad que disminuye radialmente), una com-

iv

paración entre los centroides de velocidad de estas líneas sugiere que el gas ionizado está expandiéndose.

A partir de de las tres transiciones moleculares descritas se determinó el contenido del gas molecular denso asociado a los objetos compactos del continuo centimétrico. Mediante mapas de intensidad integrados en velocidad (momento 0) se detectó $H_2CO(3_{0,3} - 2_{0,2})$ y $H_2CO(3_{2,1} - 2_{2,0})$ en 20/20 objetos, y SO en 14/20 objetos. Además, realizamos un análisis cualitativo de los perfiles moleculares para caracterizar la cinemática del gas molecular sobre 12/20 objetos cuya emisión fue inafectada por lóbulos laterales ('sidelobes', en inglés) de fuentes brillantes adyacentes. Se encontró que 3/12 parecen exhibir movimientos de caída y 9/12 movimientos de expansión. En adición, bajo la suposición de que la velocidad de H30α traza el gas ionizado más denso y cercano a la estrella, se infirió la cinemática molecular respecto a la estrella. Al comparar los centroides de H30α con los perfiles moleculares para 7/8 fuentes con detección de esa RL se encontró que la cinemática molecular para 4/7 fuentes es simétrica respecto al movimiento estelar, y para 3/7 fuentes está corrida al azul respecto al movimiento estelar.

La cinemática de expansión del gas ionizado, y la cinemática predominántemente de expansión del gas molecular, sugieren que la acreción de material a las estrellas no es dominante entre escalas de 2000 a 3000 au. Mediante dos métodos encontramos densidades electrónicas más 'altas' que las asociadas a regiones UC, pero más bajas que aquellas encontradas en regiones conocidas HII HCs de referencia. Esta discrepancia se resuelve observando que nuestra muestra reproduce la relación inversa n_e vs D observacionalmente derivada en literatura previa para múltiples muestreos de regiones HII compactas y ultracompactas (UC). Por lo tanto, nuestra interpretación es que estamos caracterizando una población más común de regiones HII HC's que los típicos objetos de referencia. Esto, en conjunto con la cinemática del gas ionizado, sugiere que estos objetos son versiones mas pequeñas de regiones UC y compactas en

expansión. La determinación del tipo espectral B temprana para la mayoria de nuestros objetos apoya esta interpretación, y es consistente con la Función de Masa Inicial (*IMF*, 'Initial Mass Function', en inglés) para estrellas en la etapa ZAMS. Especulamos sobre la existencia de dos tipos de objetos denominados como hipercompactos según sus diámetros: i) aquellos generados por estrellas, mayormente tipo B, carecientes de acreción residual y que están en expansión; ii) objetos extremadamente densos con grandes anchos de línea sub-milimétrica.

El trabajo expuesto en esta obra fue realizado por el estudiante de maestría Rudy Rivera Soto bajo la supervisión de su tutor principal Roberto Galván Madrid. El grueso de esta tesis ha sido enviado para su publicación al *Astrophysical Journal (ApJ)* bajo el título '*Recombination Lines and Molecular Gas from Hypercompact HII regions in W51 A*'. El proceso de arbitraje inició el 8 de enero de 2020. El primer ciclo de comentarios del arbitro comenzó el 8 de febrero de 2020. El segundo ciclo de comentarios del arbitro comenzó el 25 de mayo de 2020.

Abstract

We present a detailed characterization of the population of compact radio-continuum sources in W51 A using subarcsecond VLA and ALMA observations. We analyzed their 2 cm continuum, the recombination lines (RLs) H77α and H30α, and the lines of $H_2CO(3_{0,3} - 2_{0,2})$, $H_2CO(3_{2,1} - 2_{2,0})$, and $SO(6_5 - 5_4)$. We derive diameters for 10/20 sources in the range $D \sim 10^{-3}$ to $\sim 10^{-2}$ pc, thus placing them in the regime of hypercompact HII regions (HC HIIs). Their continuum-derived electron densities are in the range $n_e \sim 10^4$ to 10^5 cm^{-3}, lower than typically considered for HC HIIs.

We combined the RL measurements and independently derived n_e, finding consistent values. We found that most of the sources in our sample are ionized by early B-type stars, not O-type stars, and a comparison of n_e vs D shows that they follow the inverse relation previously derived for ultracompact (UC) and compact HIIs. When determined, the ionized-gas kinematics are always (7/7) indicative of outflow. Similarly, 9 and 3 out of 12 sources show evidence for expansion and infall motions in the molecular gas, respectively. We hypothesize that there could be two different types of *hypercompact* ($D < 0.05$ pc) HII regions: those that essentially are smaller UC HIIs, often ionized by less massive stars; and those that are also *hyperdense* ($n_e > 10^6$ cm^{-3}), probably associated with O-type stars in some specific stage of their formation or early life.

<div align="center">Contents</div>

1. Introduction

1.1. The Electromagnetic Spectrum and Radio Astronomy

Radio Astronomy is the observational science that studies the radio waves emitted by celestial sources. Fundamentally, electromagnetic (EM) radiation is comprised of electromagnetic waves – intertwined oscillations of the electric and magnetic fields – that propagate at the speed of light in space. These waves are characterized by their wavelength λ (or frequency ν) into the EM spectrum, which in practical terms ranges from $10^{-12} < \lambda < 10^8$ m ($1 < \nu < 10^{18}$ Hz). This EM spectrum is qualitatively classified into seven regions in order of increasing wavelength: gamma, x-ray, ultraviolet (UV), visible, infrared (IR), microwave, and radio. The microwave and radio part of the EM spectrum as viewed from ground-based telescopes is limited by factors such as atmospheric transparency and emissivity, receiver noise, and technological limitations, which in practice fixes the observability wavelength range to 0.3 mm $< \lambda <$ 30 m (or frequencies of 10 MHz $< \nu <$ 1 THz). This wide frequency range permits a variety of astrophysical phenomena to be observed with radio telescopes. In the following paragraphs we describe the mechanisms which produce radio emission relevant for this thesis, as well as the instruments that were used.

1.1.1. Radio emission mechanisms

The mechanisms which produce emission of EM waves can be classified as either thermal (meaning that the intensity of the radiation is dependant on the thermodynamic temperature of the emitting material), or non-thermal (meaning the opposite). Another classification scheme is dividing the radiation in either 'continuum' or 'spectral-line'. Continuum – broadband – emission is so named because the physical processes which cause it have non-quantized energy exchanges that produce photons with a continuous energy distribution, whereas spectral lines appear as narrow ($\Delta\nu \ll \nu$) emission or absorption features in a spectrum. Examples of thermal radio continuum emission are the nearly blackbody surfaces of Solar-system objects, the emission from thermalized dust grains, or, importantly for this work, the emission from free-free interactions of thermal electrons in an ionized gas – known as

'bremsstrahlung' or braking radiation, see figure 1 –. Examples of thermal line emission in the radio are atomic transitions such as the 21 cm line due to neutral Hydrogen spin flip, recombination lines of Hydrogen and heavier atoms, and thermalized transitions of molecules such as CS, CO, H_2CO, or SO, the latter two being used in this work. Examples of non-thermal radio emission are the synchrotron radiation[1] emitted by active galactic nuclei and quasars, which depends on factors like the strength of magnetic fields, as well as gyrosynchrotron[2] radiation from YSOs, maser[3] emission from molecules and atoms, scattering processes, etc. On Galactic scales, thermal emission dominates the radio sky at short radio wavelengths (high frequencies), with $\lambda < 0.1$ cm ($\nu > 300$ GHz) mostly due to emission from dust grains, and free-free having a significant contribution in the range $0.3 < \lambda < 30$ cm (1 GHz $< \nu < 100$ GHz). Non-thermal continuum emission often dominates at long wavelengths $\lambda > 10$ cm ($\nu < 3$ GHz).

Observations of recombination line emission are important in this work. This phenomenon occurs when an electron recombines at any excited level of hydrogen and initiates a radiative cascade that culminates in the ground state. Spectral lines are generally expressed in terms of a line profile function ϕ, which describes the emission or absorption distribution around the central frequency ν_0 of the transition and which peaks at the same frequency. The width of this distribution, the so called spectral line width $\Delta\upsilon$, can be subject to broadening due to a variety of local effects. Natural broadening occurs in proportion to the spontaneous decay rate A_{10} of an excited state. Its line profile function is a Lorentzian of the form $\phi(\nu) = \frac{A_{10}}{4\pi} \frac{1}{(\nu-\nu_0)^2+(A_{10}/4\pi)^2}$, with a full-width at half-maximum power (FWMH) defined as $\Delta\upsilon_{FWHM} = A_{10}/2\pi$. Doppler broadening occurs due to the thermal motions and velocity distributions of atoms, which depend on the temperature and dynamical bulk (ordered or turbulent) motions, respectively. Its line profile function is a Gaussian of the form $\phi(\nu) = \frac{1}{\sigma\sqrt{2\pi}}\exp(-(\nu - \nu_0)^2/\sigma^2)$, with standard deviation σ and

---

[1] Can be produced by relativistic, charged particle subject to an acceleration perpendicular to their velocity, such as within magnetic fields.

[2] Same as the prior example, but for non-relativistic particles.

[3] Stimulated emission due to an inversion populated system of atoms or molecules.

3

a FWHM defined as $\Delta v_{FWHM} = 2\sqrt{2\ln 2}\sigma$. The thermal and dynamical components can combine in quadrature to form the total (Gaussian) Doppler broadening component, $\Delta v_G^2 = \Delta v_{thermal}^2 + \Delta v_{dynamical}^2$. Finally, pressure broadening occurs due to particle collisions and its line profile is, similarly as to the Natural broadening, also a Lorentzian. The line profile of a spectral line which is broadened by both the Gaussian and Lorentzian components is a convolution of them both and is called a Voigt profile, whose full width half max can be expressed algebraically as in eq. 7 (Gordon & Sorochenko 2002; Keto et al. 2008; Galván-Madrid et al. 2012). Further details on the relevant RL analysis used in this work are shown in §3.2. In addition to derivation of physical properties associated to line broadening, comparisons between the velocity of various RLs, which can trace different regions of the ionized gas, can help infer the bulk ionized gas kinematics.

The molecular gas content of a region can be explored by observing transitions of various molecules. Such transitions can be rotational, vibrational, or ro-vibrational. These can be visible in emission if the molecule is above its critical density, in which case the excitation temperature approximates the gas kinetic temperature. This is known as a thermalized transition. Certain tracer molecules are used to identify a variety of regions. High critical density molecules such as CS can detect the presence of cores, while an entire cloud can be detected with CO. Further details regarding the molecular tracers used in this work are given in §5.

1.1.2.   Radio interferometry basics

Observations of the radio spectrum can be achieved using one of two instruments: 1) a single dish telescope, or 2) a radio interferometer. Examples of these instruments are shown in figure 2. Although single dish radio telescopes can have large geometric 'photon collecting' areas, and thus high sensitivities, they suffer from a slew of practical issues which can make the use of interferometers more favorable in some circumstances. For instance, the angular resolution θ is given by $\theta \approx \lambda/D_t$, which would require that the telescope diameter D_t be very large to reach sub-arcsecond resolutions. Material limitations restrict single-dish telescopes from having diameters
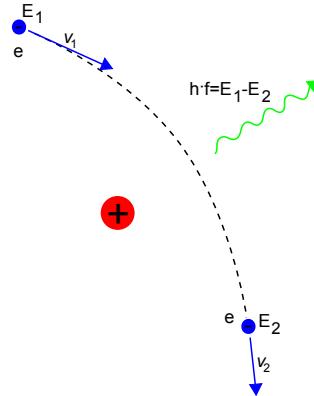
Figure 1. Diagram illustrating the free-free emission mechanism. A proton, $+$, is approached by a free electron, e, at initial velocity v_1 and kinetic energy E_1. The Coulomb interaction between them deflects the electron to a velocity v_2 and kinetic energy E_2. The process releases a photon with energy equivalent to the energy loss of the electron.

larger than about 500 m. This can be overcome through the use of interferometers, which are comprised of various ($N \geq 2$) smaller-dish antennas performing measurements in conjunction. The spacing of the antenna elements, so called baseline vectors b, allows interferometers to achieve high resolving power by covering apertures as large as a single dish whose diameter is equivalent to the maximum baseline, albeit at the cost of sensitivity. In addition, performing reasonable photometric measurements and imaging requires pointing accuracies σ_a within $\sigma_a \approx \theta/10$. Yet, pointing accuracy depends on the mechanical tracking accuracy of the beam direction, which is affected by external factors relating to the sheer size of a large single dish, such as sagging due to gravity, expansion due to heating, or torques due to winds. The various advantages of interferometers over single dish telescopes make them the desired option for observing the radio sky in many circumstances. What follows is a discussion on basic antenna and interferometer theory, and a delineation of the technical aspects of the VLA and ALMA interferometers used in this study.

An antenna is, at its simplest, a set of two colinear conductors separated by a current source. This antena, called a dipole (of length $l < \lambda$), converts currents I (or voltages V through Ohm's law, $V = IR$, for a resistance R) into EM waves in the case of transmitters, or vice-versa in the case of receivers. A pair of crossed

Figure 2. Photos of the Arecibo radio telescope[a] (top), and of the VLA[b] (middle) and ALMA[c] (bottom) interferometric arrays.

[a]   Image Credit: https://www.naic.edu/ao/photos
[b]   Image Credit: https://public.nrao.edu/gallery/topic/radio-telescopes/
[c]   Image Credit: ESO/C. Malin

dipoles can simultaneously collect power from two orthogonal polarizations of an EM wave. Two antenna diagrams are shown in figure 3. A transmitting antenna can be characterized by its peak power gain $G_0 = 4\pi/\Omega_A$, equal to the power transmitted through its beam solid angle Ω_A. A receiving antenna can be characterized by its effective collecting area $A_e = 2P_\nu/S_\nu$, equal to its output spectral power P_ν in response to the flux density S_ν from an unpolarized point source. For any lossless antenna, conservation of energy requires that their direction averaged gain be unity, $\langle G \rangle = 1$, and consequently that $\int_{sphere} G d\Omega = 4\pi$, and also for any such antenna, their average collecting area is the same and only wavelength dependent, $\langle A_e \rangle = \lambda^2/4\pi$. The reciprocity between receiving/transmitting antennas can be weakly stated as $G(\theta, \phi) \propto A_e(\theta, \phi)$, meaning that the power pattern of an antenna is the same for transmitting and receiving, or more strictly as $V_A I_A = V_B I_B$, meaning that, for an (A, B) antenna pair, a current I_B measured at B due to a voltage V_A applied to A, will be the same as the current I_A measured in A for an equal voltage V_B applied to B, in both the phase and amplitude which characterize the the received/transmitted signal. By combining energy conservation principles along with the weak reciprocity theorem (as previously defined), the relationship between the transmitting and receiving power patterns for any antenna can be stated as $A_e(\theta, \phi) = \lambda^2 G(\theta, \phi)/4\pi$. Thus one can use the transmitting power pattern to determine the effective collecting area of a transmitting antenna when used as a receiver, or vice versa for a receiving antenna when used as a transmitter.

Most radio telescopes use reflectors, commonly of paraboloid shape, to collect and focus a plane wave from a distant source into feed antennas connected to receivers at their focal point. Arrays of these types of antennas are advantageous over arrays of dipoles, primarily because their effective collecting area may approach their projected geometric area $A = \pi D^2/4$, with D the reflector diameter, and also because they can operate over a wide frequency range. In order for the reflector to focus the waves on-axis and in phase, the received wavefront must be nearly planar. Although the EM waves emitted by a source are spherical, it is justifiable to consider them planar if the distance to the source is much larger than the moderately arbitrary definition

1.1 The Electromagnetic Spectrum and Radio Astronomy
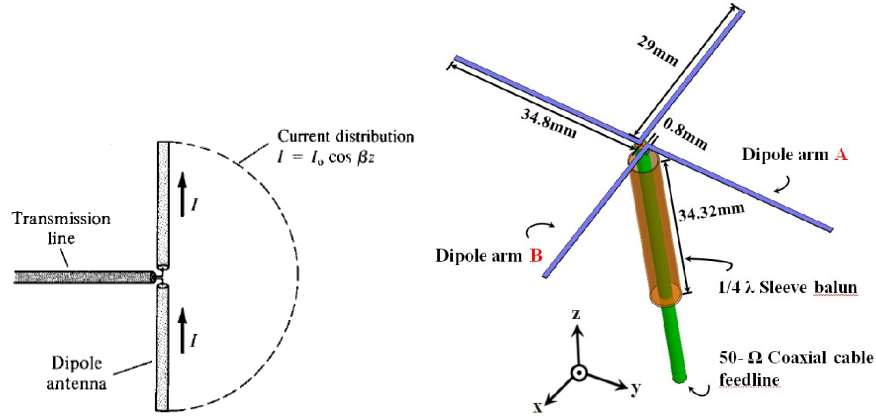
Figure 3. Diagrams of the simple dipole antenna (left) by Lodro (2016) and the crossed dipole antenna (right) by Chou et al. (2013). In the simple dipole antenna diagram appear the two colinear conductors separated by and connected to a current source via a transmission line. In the crossed dipole antenna diagram two dipole arms A and B are crossed and similarly connected to the current source.
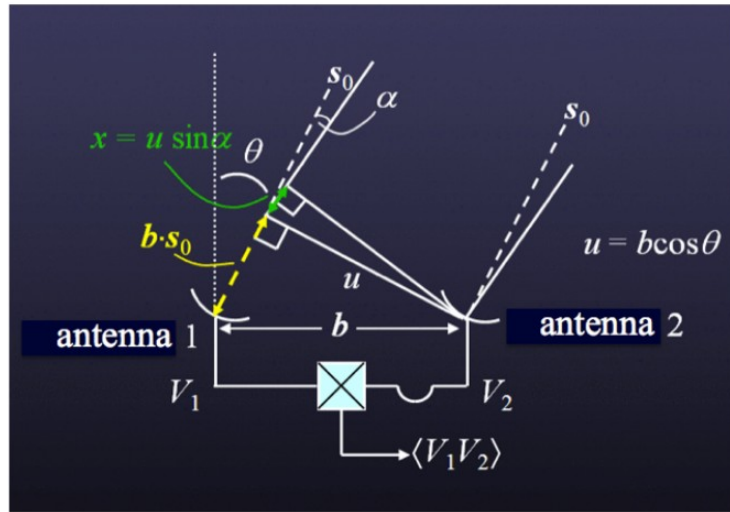
Figure 4. Diagram of ideal interferometer in 1D with two antenna elements, separated by a baseline, b, both pointing towards a source s_0 at an angle θ from the meridian, and connected to a correlator which combines the voltages (Remijan et al. 2019).

of far-field distance $R_{ff} \approx 2D^2/\lambda$. In such a case, and under the approximation that the distance is also much larger than the aperture size, the beam (power) pattern,

or power gain of an aperture antenna can be defined as the Fourier transform[4] of the electric field illuminating the antenna. Weak reciprocity implies that this is also true of the receiving power pattern of an aperture antenna, in which it represents the point-source response. The central peak of the power pattern is known as the main or primary beam, while the smaller adjacent peaks are called sidelobes. The angular size of the main beam is characterized in terms of the Half-Power Beam Width (HPBW) or equivalently the previously defined FWHM, is given as $\theta_{HPBW} \propto \lambda/D$, and is also known as the resolving power.

Interferometry consists in the combination of any number of physically separated antenna elements in order to receive celestial signals. The sky brightness distribution can be sampled on smaller angular scales (better resolution) than with a single antenna dish by interfering the signals from the multiple elements via a technique called aperture synthesis, which is described in the following[5].

Typically, most observed emission will not be received on-axis by any antenna pairs separated by a baseline distance vector b. Thus from the perspective of a source located at an angle θ from the meridian, and an orthogonal reference angle φ, the projected antenna pair separation is given by $u = b_1 \cos(\theta)$ and $v = b_2 \cos(\varphi)$ in 2D, with baseline components b_1, b_2. A simpler, 1D diagram of this scenario is shown on figure 4. This projected separation means that there is a geometric delay between the emission received by different antennas, an effect which can be corrected electronically. Any off-axis signal reaching an antenna pair can be described by two orthogonal small-angles α and β which introduce additional path length components $x = u \sin(\alpha) = ul$, $y = v \sin(\beta) = vm$, with u and v orthogonal spatial frequency components, and hence phase differences between the pair. These signals can be characterized in terms of the voltage response of both antennas and a phase delay factor, as $V_2 = V_1 e^{2\pi i(ul+vm)}$. These voltage responses are then multiplied and time-averaged by a correlator device and, provided the received signals are incoherent,

---

[4] A type of integral transform, and mathematical operation which converts a function represented in the time-domain to one represented in the frequency-domain.

[5] Adapted from Condon & Ransom (2016) and Remijan et al. (2019)

result in $\langle V_1 V_2 \rangle \propto \int \int \langle V_1(l,m)^2 \rangle e^{2\pi i(ul+vm)} dl dm$. Yet, since $V^2 \propto P$, and the received spectral power P_ν of a telescope of effective area A_e is $P_\nu = \frac{1}{2} I_\nu A_e \delta \Omega$, with I_ν specific intensity and $\delta \Omega$ solid angle, then the correlated voltage responses can be expressed as $\mathcal{V}(u,v) = \int \int I(l,m) e^{2\pi i(ul+vm)} dl dm = A e^{i\phi}$. This is known as a complex visibility, characterized in terms of an amplitude A, which relates to the brightness, and a phase ϕ, which relates to the source location relative to the phase center.

The van Cittert-Zernike theorem dictates how the complex visibility distribution relates to the sky brightness distribution, with the former being the Fourier transform of the latter, and vice-versa. Thus, the sky brightness distribution can be recovered from measurements of the complex visibilities in the (u,v) plane. It follows, then, that approximating the true sky brightness distribution requires increasing the (u,v) plane sampling. This can be achieved in a number of ways, for example, adding more antennas at differing distances to obtain more baselines and hence more samples, repeated observations as the Earth rotates such that the change in projected antenna separations produces more samples, and using different antenna configurations to sample different parts of the plane. If the source emission is reasonably constant, then the (u,v) plane can be well sampled and an approximating image of the true sky brightness distribution can be produced.

1.1.3.   The VLA and ALMA interferometers

This study makes use of two radio interferometric[6] telescopes, being the Very Large Array (VLA) and the Atacama Large Millimeter Array (ALMA). The VLA[7] is an array composed of 27 antenna elements, each of 25 m diameter, arranged into a 'Y' shape having 9 elements on each arm. Each antenna has eight receiver bands which provide continuous coverage from 0.6 cm to 30 cm (1 - 50 GHz) of successively shorter wavelengths (higher frequencies), denoted as bands L, S, C, X, Ku, K, Ka, and Q. They also have longer wavelength receivers such as the 0.6 m to 1.3 m (230 - 470

---

[6] Interferomeners are essentially fourier filters which recover emission in a range of scales set by the maximum and minimum baseline lengths, which determine angular resolution and the maximum scale of recoverable emission of an image, respectively.

[7] Details and notation according to its respective documentation (Momjian 2017).

MHz) P-band and the 3.5 m to 5.6 m (54–86 MHz) 4-band. Motorized transporters can move the antennas along rail tracks into four different basic configurations of successively decreasing baseline separations, called A, B, C, and D, each with their respective angular resolutions θ_{HPBW} and largest (recoverable) angular scales θ_{LAS} for a given observing band. The stated configurations have maximum baseline separations of 36.4, 11.1, 3.4, and 1.03 km, respectively, and minimum baseline separations of 0.68, 0.21, 0.035, and 0.035 km, respectively. Observations with larger baseline separations and shorter wavelength bands result in better angular resolutions, yet worse largest recoverable angular scales. Therefore, Q-band observations in the (most extended) A configuration produce the absolute highest angular resolution reached with the VLA of $\theta_{HPBW} = 0.043''$, and a corresponding value of $\theta_{LAS} = 1.2''$. Conversely, within the bands of continuous coverage, L-band observations in the (most compact) D configuration produce its absolute largest recoverable scale of $\theta_{LAS} = 970''$, with corresponding value of $\theta_{HPBW} = 46''$. Larger angular scales, however, can be recovered using the P- or 4- bands.

The ALMA[8] radio telescope, on the other hand, has a main array consisting of fifty antenna elements of 12 m diameter, used for sensitive high-resolution imaging, a more compact secondary array consisting of twelve 7 m diameter antennas, and four 12 m single dishes. The telescope is currently on its seventh operation cycle (Cycle 7), and offers eight receiver bands of successively shorter wavelengths, numbered 3 - 10, which can cover most wavelengths in a maximum range from 3.6 mm to 0.32 mm (84 - 950 GHz). The main array can be arranged into ten different configurations of successively increasing baseline separations, denoted C43-1 through C43-10, each with their respective angular resolutions θ_{res} and maximum recoverable scales θ_{MRS} for a given observing band. Observations in the highest available band (Band 7), and in the most extended configuration of 8.69 km, taken as the 80th percentile value of the maximum baseline (16.2 km), can produce the absolute highest angular resolution reached with ALMA, of $\theta_{res} = 0.012''$, with corresponding $\theta_{MRS} = 0.144''$.

---

[8] Details and notation according to its respective documentation (Remijan et al. 2019)

Conversely, Band 3 observations in the most compact configuration of 21.4 m, taken as the 5th percentile value of the minimum baseline (14.6 m), can produce its absolute maximum recoverable scale of $\theta_{MRS} = 28.5''$, with corresponding $\theta_{res} = 3.38''$. Smaller separations can be filled in using the 7 m array, which in Band 3 gives $\theta_{MRS} = 66.7''$, with corresponding $\theta_{res} = 12.5''$.

In this work, we use VLA observations in the 2 cm (15 GHz) Ku band, in configurations D ($\theta_{\text{HPBW}} = 4.6''$, $\theta_{\text{LAS}} = 97''$) and B ($\Theta_{\text{HPBW}} = 0.42''$, $\theta_{\text{LAS}} = 12''$). In addition we use Cycle 2 ALMA observations in the 1.3 mm (230 GHz) Band 6, in two 12 m array configurations ($\theta_{\text{res}} = 0.2''$). Further observational details are provided in §2.

1.2.   Giant Molecular Clouds and Star Formation

Star formation is a process which is carried out inside giant molecular clouds (GMC's) within the interstellar medium of a galaxy, in what are known as 'star-forming regions' (Shu et al. 1987). They are named as such due to the majority of the hydrogen being in molecular form H_2. The Milky Way is host to many such clouds, from the less massive Taurus Molecular Cloud with $\sim 10^4 M_\odot$ (Pineda et al. 2010), to the W49 A Molecular Cloud with $> 10^6 M_\odot$ (Galván-Madrid et al. 2013). The W51 molecular cloud complex is one of the most massive and copiously star-forming regions in the galaxy. GMCs have diameters ranging from 5 to 200 pc, have masses ranging from 10^4 to $10^6 M_\odot$ and temperatures averaging tens of Kelvins.

Before a star reaches its optically visible, main sequence stage, there exists an embedded phase lasting a fraction of their lifetime (Churchwell 2002). This phase divides into various objects that have been observed at mid-infrared (mid-IR) radio wavelengths (Menten et al. 2005; van der Tak & Menten 2005). The first are dense IR dark clouds, that is, clouds seen in absorption against the mid-IR background emission, whose density maxima and temperature minima probably constitute the initial conditions of high-mass star formation. They house filamentary structures which can compress into cold massive cores via self-gravitation and/or shock compression due to convergent turbulent gas streams where star formation can initiate. This is followed

by a stage of gravitational collapse of some of these cores into protostellar objects. These are gaseous objects in quasi-hydrostatic equilibrium, that is, in which the internal gas pressure balances the gravitational force. In this stage objects called Hot Molecular Cores (HMCs) can form. They have sizes of < 0.1 pc and temperatures larger than 100 K, and can be observed in emission via various molecular tracers (such as CO, HCO^+, H_2CO, and others) due to internal heating by the protostar. Once the star reaches the Zero-Age Main Sequence (ZAMS) the hydrogen burning phase begins and the star enters a stage of disruption of its parent cloud, which occurs through its winds, outflows, and of particular importance to this work, ultraviolet (UV) radiation. This ionizing radiation produces the compact HII regions which are the target of this study.

1.3.   HII Regions

Massive stars form in the densest clumps within GMCs, mostly in a clustered manner (for a recent review see Motte et al. 2018). They gain mass via accretion and eventually reach the ZAMS. The mass at which this happens is in the range $M_{ZAMS} \sim 10 - 30$ $M_\odot$, depending on geometry and rate of (proto)stellar accretion (Hosokawa et al. 2010). When the ZAMS is reached the powerful ultraviolet radiation from their hot stellar atmospheres are enough to ionize their own accretion flows and the surrounding gas, generating an HII region (Keto 2003, 2007; Peters et al. 2010a; Tanaka et al. 2016). These regions are initially small, dense, and surrounded by a dusty, denser layer of gas. Their size is determined by the overall ionization balance, that is, the balance between photo-ionization and the radiative recombinations of free (thermal) electrons. In order of descending density (or ascending size) the HII regions are called hypercompact (HC), ultracompact (UC), or compact. The simplest interpretation of the relation between hypercompact (HC) and ultracompact (UC) HII regions is that they are successive stages in the early evolution of ionization soon after massive stars reach the ZAMS (Wood & Churchwell 1989; Kurtz et al. 1994; Hoare et al. 2007). However, models and simulations show that some HC HII's are associated with active accretion (Keto 2007; Peters et al. 2010a,b), and that early

HII region evolution can be a time-variable process where the size is not necessarily a predictor of the absolute age (Galván-Madrid et al. 2011; De Pree et al. 2014). These regions can be observed and imaged at 1000 au resolutions via some of their characteristic emission, such as the free-free radio continuum of the ionized gas (a significant contributor within $0.3 < \lambda < 30$ cm), continuum emission by dust, or their hydrogen recombination lines (RLs). HC HIIs are typically faint and deeply embedded. Therefore, most of our observational knowledge about them, such as their sizes and fluxes, is based on their cm continuum properties (Sánchez-Monge et al. 2011; Ginsburg et al. 2016; Rosero et al. 2016; Yang et al. 2019). These continuum parameters can then be used to determine emission measures and electron densities (see eqs. 3a, 3b). In addition, the surrounding molecular gas envelope can be observed via rotational transitions of molecular tracers such as H_2CO and SO.

Further characterization of their Hydrogen RLs is helpful to assess the densities and kinematics of the HII regions, which in turn gives additional insight into their physical nature (e.g., Sewilo et al. 2004; Guzmán et al. 2014). Earlier interferometric studies were able to detect (sub)mm RLs only in the brightest HC HIIs (e.g., Keto et al. 2008; Galván-Madrid et al. 2009; Shi et al. 2010b). With ALMA it is now possible to go much deeper (e.g., Peters et al. 2012; Klaassen et al. 2018; Zhang et al. 2019) and characterize larger samples.

1.4.   The W51 Molecular Cloud complex

The W51 molecular cloud complex was first observed on the 22 cm Galactic plane survey performed by Westerhout (1958). It is composed of three main bright radio regions, being the eastern component W51 A, the western component W51 B, and the southern component W51 C, as seen on figure 5. This represents one of the most massive - $M \geq 10^6 M_\odot$ (Combes 1991) - and luminous - $L_{IR} \geq 10^4 L_\odot$ (Urquhart et al. 2014) - star-forming regions from our galaxy. The set of the *W51 Main / IRS1* (previously G49.5-0.4) and *W51 North / IRS2* (previously G49.4-0.3) regions make up the main star formation site known as the W51 A complex. This region has been studied in detail in the past, mostly in the cm radio (e.g., Gaume et al. 1993;
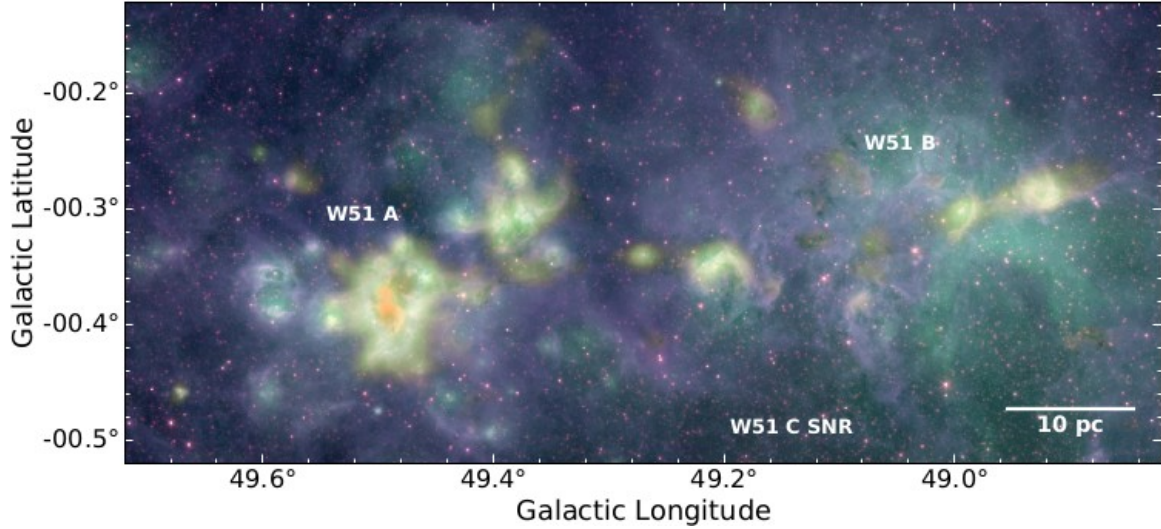
Figure 5. Color composite image of W51 with regions W51 A, B, and C, adapted from Ginsburg et al. (2015). The blue, green, and red colors are WISE bands 1, 3, and 4 (3.4, 12, and 22 μm, respectively), the yellow-orange colors are from the Bolocam 1.1 mm Galactic Plane Survey (Aguirre et al. 2011), and the faint white color is from a 90 cm VLA image by Brogan et al. (2013).

Mehringer 1994; Ginsburg et al. 2016), (sub)mm (e.g., Zhang et al. 1998; Ginsburg et al. 2017), infrared (e.g., Kang et al. 2009; Saral et al. 2017), and X-rays (e.g., Townsley et al. 2014). Distance measurements by parallax to masers in this complex produce values of $5.41^{+0.31}_{-0.28}$ kpc for the radio-continuum source subcluster e2/e8 (Sato et al. 2010) and $5.1^{+2.9}_{-1.4}$ kpc for IRS2 (Xu et al. 2009). The distances place this region in the mid-plane of the galaxy within the Carina-Sagittarius arm, as shown in figure 6.

1.4.1. W51 A

The main object of this study is W51 A. Observations made by Mezger & Henderson (1967), Gardner & Morimoto (1968), and MacLeod & Doherty (1968) grouped the components of W51 into north and south. The first of these groups, which contains regions G49.5-0.4 and G49.4-0.3, was observed in its 5 GHz continuum emission by Martin (1972). He named eight components as W51 a-h, within G49.5-0.4, the brightest region in W51 A. Subsequent studies with better resolution conducted by Scott (1978) in the radio continuum at 5 GHz and 15 GHz on the strongest of these

components, W51 e and W51 d, resolved the two compact sources e1 and e2. In addition, observations in the VLA configuration A by Gaume et al. (1993) at 3.6 cm and 1.3 cm identify the point source d2, and also the sources e3, e4 and e5. Observations in the C and D configurations of the VLA by Mehringer (1994) at 3.6 cm, 6 cm, and 20 cm identify several bright HII regions, including the source called e6. Measurements of recombination lines allowed derivation of the electron temperature of the region ($T_e \approx 7500K$). High angular resolution studies ($0.2'' - 1.0''$) in the VLA configuration C revealed the source called e8 (Zhang & Ho 1997). W51A observations made by Ginsburg et al. (2016) between 2 GHz and 16 GHZ with resolution between $0.3'' - 0.5''$ catalog several new compact sources in the continuum, named as e9-e23, and also divide source e8 in two components: e8n and e8s. All of the aforementioned sources can be seen in figure 7.

Studies on some of these HII regions have shown evidence of gas infall, indicative of accretion (Zhang & Ho 1997; Zhang et al. 1998; Young et al. 1998; Keto & Klaassen 2008), although observations by Shi et al. (2010a) and Goddi et al. (2016) suggest that the material is moving preferentially towards *"Hot Molecular Cores"* (HMC's) adjacent to the HII regions. Previous observations in the sub-millimeter have only been able to identify the brightest hypercompact HII regions, however, higher resolution studies with ALMA allow us to more easily characterize the stellar population of the region.
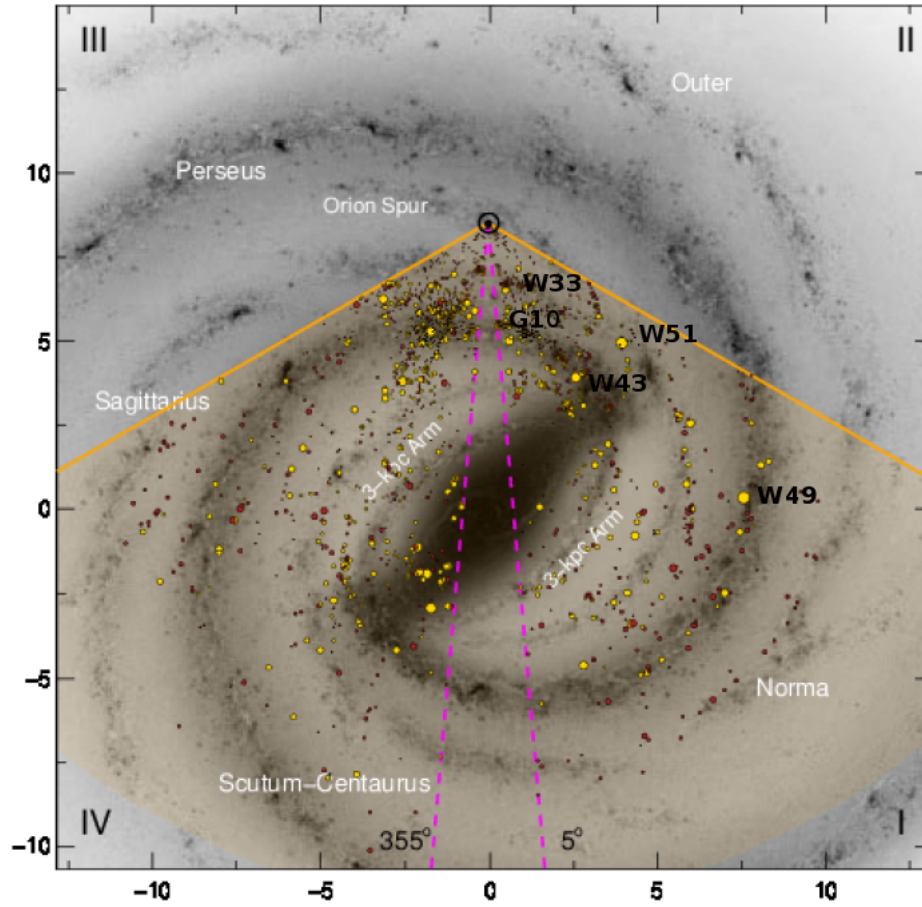
Figure 6. Diagram of Giant Molecular Clouds within the Milky Way galaxy in the galactic coordinate system. Named are the W51, W49, W43, W33, and G10 GMCs. W51 lies in the galactic mid-plane within the Carina-Sagittarius spiral arm.

2. Data

2.1. Observational Data

The VLA Ku-band observations were executed for a total time of 1 hour in D-configuration on March 02, 2013, plus 5 hours in B-configuration on October 01, 2013. The observations were made under program 13A-064 and were originally reported in Ginsburg et al. (2016). We use the 2 cm continuum and Hydrogen 77α RL images and refer the reader to their paper for details on the observations and data reduction. The continuum image has a central frequency $\nu_{0,\mathrm{cm}} = 13.436$ GHz (2.2 cm), an rms noise of about 50 μJy beam^{-1}, and a synthesized beam FWHM $0.34'' \times 0.33''$, P.A. $= 14.8°$. The H77α cube ($\nu_{0,\ \mathrm{H77}} = 14.129$ GHz) was created with uniform weighting, has a channel width of 1.33 km s^{-1}, a velocity range from -207.9 km s^{-1} to 288.0 km s^{-1}, and a synthesized beam FWHM of $0.39'' \times 0.34''$, P.A. $= 75.6°$. The typical rms noise in channels with bright emission is 0.46 mJy beam^{-1}, whereas in channels free of emission it is about 0.32 mJy beam^{-1}.

The ALMA observations were executed as part of Cycle 2 project 2013.1.00308.S in two 12m-array configurations. We refer to Ginsburg et al. (2017) for details on the data reduction. The H30α ($\nu_{0,\mathrm{H30}} = 231.901$ GHz) cube has a channel width of 1.2 km s^{-1}, a velocity range from 25.0 km s^{-1} to 93.4 km s^{-1}, and a synthesized beam FWHM of $0.32'' \times 0.31''$, P.A. $= 50.7°$. The typical rms noise in all channels is about 3.53 mJy beam^{-1}.

To allow for a uniform comparison between tracers of ionized gas, we regridded both the 2 cm continuum and H77α images to pixel dimensions of $0.05''$, matching those of the ALMA images, and afterwards convolved the 2 cm continuum, H77α, and H30α images to a common circular beam with FWHM$= 0.40''$. We use the convolved images in the analysis of these tracers unless otherwise specified.

We also use the molecular-line cubes from the data release of Ginsburg et al. (2017). The lines of interest are: $H_2CO(3_{0,3} - 2_{0,2})$ at $\nu_0 = 218.22219$ GHz, $H_2CO(3_{2,1} - 2_{2,0})$ at $\nu_0 = 218.76007$ GHz, and $SO(6_5 - 5_4)$ at $\nu_0 = 219.94944$ GHz. The $H_2CO(3_{0,3} - 2_{0,2})$ cube has a channel width of 0.17 km s^{-1}, a velocity range from 20

18

Table 1. Source Catalogs

Catalog Name (# of sources)	Sources
A (29)	d2, d4e, d4w, d5, d6, d7, e1, e2, e3, e4, e5, e6, e8n, e8s, e9, e10, e11, e12, e13, e14, e15, e16, e17, e18, e19, e20, e21, e22, e23
B (20)	d2, d6, d7, e1, e2, e3, e4, e5, e6, e8n, e8s, e9, e10, e12, e13, e14, e20, e21, e22, e23
B-H30 (8)	d2, e1, e2, e3, e4, e5, e6, e8n
B-H77 (8)	d2, e1, e2, e3, e4, e5, e6, e9
B-H30-H77 (7)	d2, e1, e2, e3, e4, e5, e6

km s^{-1} to 89 km s^{-1}, and a synthesized beam FWHM of $0.68'' \times 0.53''$, P.A. $= -66.0°$. The $H_2CO(3_{2,1} - 2_{2,0})$ cube has a channel width of 0.67 km s^{-1} and the same velocity range and beam size as the previous formaldehyde cube. The $SO(6_5 - 5_4)$ cube has a channel width of 0.67 km s^{-1}, a velocity range from -0.1 km s^{-1} to 130.1 km s^{-1}, and a synthesized beam FWHM of $1.23'' \times 1.00''$, P.A. $= -70.2°$. We retrieved atomic and molecular parameters from *Splatalogue*[9], mainly taking the laboratory measurements from the Cologne Database for Molecular Spectroscopy (CDMS) (Müller et al. 2005).

2.2.   Source Selection

We produce a sensitivity-limited sample of small UC and HC HIIs in W51 A. We first impose a size cut to the catalog of Ginsburg et al. (2016) and take only the cm continuum sources with radii $< 1''$, which corresponds to 0.026 pc at a distance of $d = 5.4$ kpc (Sato et al. 2010). This size limit roughly corresponds to the threshold

---

[9] https://www.cv.nrao.edu/php/splat/
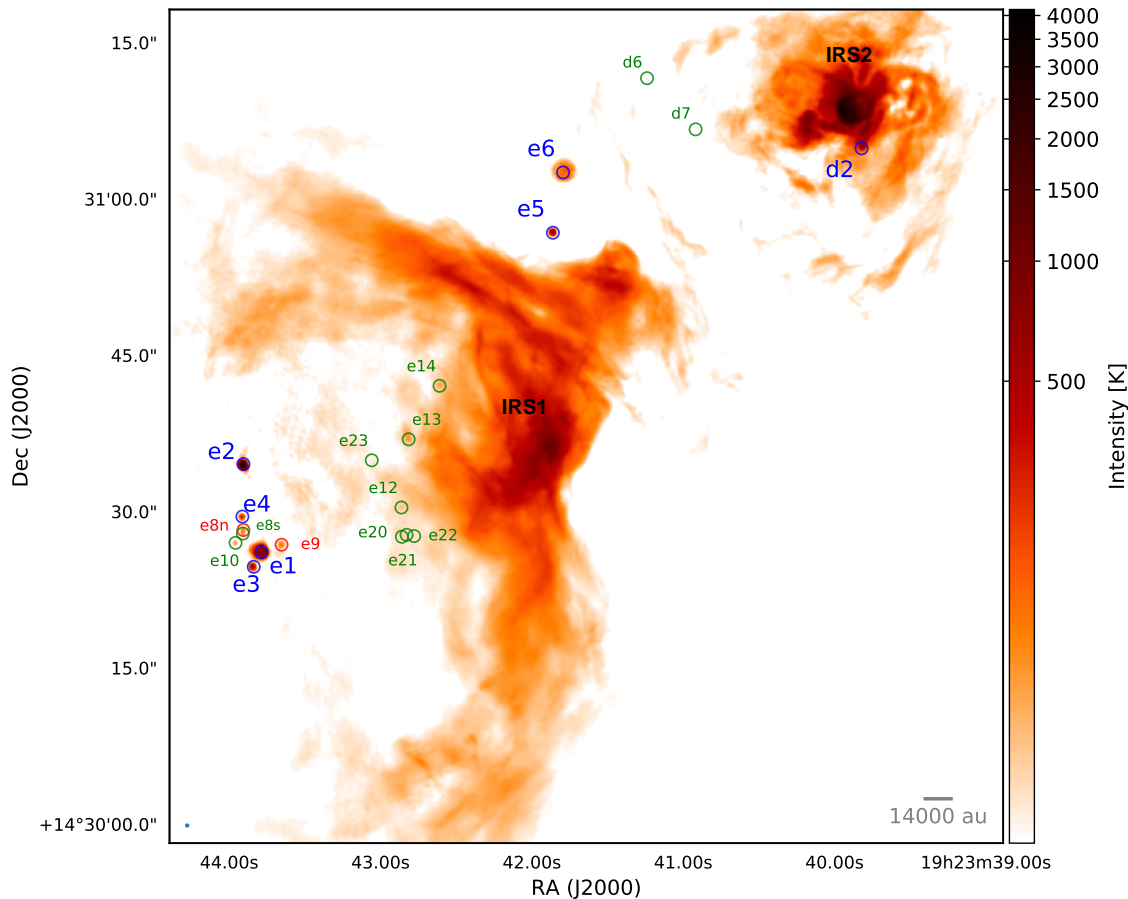
Figure 7. VLA image of the 2 cm continuum in brightness temperature [K] units. All labeled sources are compact objects in catalog B. Sources labeled in *blue* are also detected in both RLs. Sources in *red* are detected only in a single RL. Sources in *green* have no RL detection. The FWHM is $0.40''$ and the *rms* noise is about 4.8 K in locations away from bright emission. The large regions of bright emission known as IRS1 and IRS2 are labeled.

definition of HC HIIs (Kurtz 2005). The resulting catalog A is composed of 29 objects (see table 1). Since we need both cm and mm RLs for our analysis, we select from catalog A those sources that lie within the smaller ALMA field of view to define a new catalog B. The positions of these sources are shown in table 2. Then we extracted the RL spectra from sources in B and group the H77α and H30α detections in catalogs B-*H77* and B-*H30*, respectively. The intersection of the previous two catalogs is defined as B-*H30*-*H77*, to which we limit our main RL analysis.

Table 2. Source positions of 2 cm continuum image

Sources	RA	Dec
	[h:m:s]	[°: ′: ″]
d2	19:23:39.821 ± 0.002	+ 14:31:05.03 ± 0.04
d6	19:23:41.238 ± 0.001	+ 14:31:11.58 ± 0.01
d7	19:23:40.919 ± 0.001	+ 14:31:06.58 ± 0.02
e1	19:23:43.785 ± 0.002	+ 14:30:26.11 ± 0.03
e2	19:23:43.906 ± 0.0002	+ 14:30:34.48 ± 0.003
e3	19:23:43.842 ± 0.0001	+ 14:30:24.72 ± 0.002
e4	19:23:43.913 ± 0.0001	+ 14::30:29.49 ± 0.002
e5	19:23:41.863 ± 0.0001	+ 14:30:56.73 ± 0.001
e6	19:23:41.785 ± 0.002	+ 14:31:02.56 ± 0.03
e8n	19:23:43.906 ± 0.001	+ 14:30:28.17 ± 0.02
e8s	19:23:43.907 ± 0.0003	+ 14:30:27.91 ± 0.01
e9	19:23:43.654 ± 0.001	+ 14:30:26.81 ± 0.02
e10	19:23:43.958 ± 0.0003	+ 14:30:26.98 ± 0.005
e12	19:23:42.861 ± 0.001	+ 14:30:30.41 ± 0.01
e13	19:23:42.819 ± 0.002	+ 14:30:37.11 ± 0.03
e14	19:23:42.605 ± 0.001	+ 14:30:42.11 ± 0.02
e20	19:23:42.857 ± 0.001	+ 14:30:27.72 ± 0.01
e21	19:23:42.848 ± 0.001	+ 14:30:27.69 ± 0.01
e22	19:23:42.781 ± 0.0004	+ 14:30:27.67 ± 0.01
e23	19:23:43.058 ± 0.0004	+ 14:30:34.92 ± 0.01

NOTE—These are the positions of the 20 compact, 2 cm continuum sources in Catalog B.

3. cm Continuum and Recombination Lines

3.1. 2 cm Continuum

The derived size parameters obtained for the sources in catalog B are detailed in table 3, while the properties derived from the cm continuum are given in table 4. We performed an interactive 2D Gaussian fitting in CASA v.5.3.0-143 (McMullin et al. 2007) on each source to obtain their FWHM convolved and deconvolved size components along their major θ_{maj} and minor θ_{min} axes. From these we define our convolved and deconvolved sizes as the respective geometric mean of the components (Eq. (1a)). Then we calculate the convolved source size $N_{\mathrm{B,conv}}$ in beam units (Eq. (1b)) and the deconvolved physical size D in pc (Eq. (1c)):

$$\Theta = \sqrt{\theta_{\mathrm{maj}} \cdot \theta_{\mathrm{min}}}, \tag{1a}$$

$$N_{\mathrm{B,conv}} = \left(\frac{\Theta_{\mathrm{conv}}}{\Theta_{\mathrm{beam}}}\right)^2, \tag{1b}$$

$$D \approx d \cdot 4.84 \times 10^{-6} \Theta_{\mathrm{deconv}}, \tag{1c}$$

where d = 5400 pc and Θ_{deconv} is in arcsec.

To obtain the peak intensities I_{pk} and flux densities S we subtract the local background emission by estimating the average local background intensity $\langle I_{\mathrm{bg}} \rangle$ in Jy beam^{-1} as the average intensity in a ring around the source selected with polygons using the CASA viewer to avoid emission from other sources. Then, the background-subtracted flux density is estimated as $S_{-\mathrm{bg}} = S - \langle I_{\mathrm{bg}} \rangle N_{\mathrm{B,conv}}$, where S is the source flux density before subtraction.

We define our sources to be resolved if $\Theta_{\mathrm{deconv}} > 2\Theta_{\mathrm{beam}}$ (sources e1, e6), marginally resolved if $\Theta_{\mathrm{beam}} < \Theta_{\mathrm{deconv}} < 2\Theta_{\mathrm{beam}}$ (sources d7, e9), and unresolved if $\Theta_{\mathrm{deconv}} < \Theta_{\mathrm{beam}}$ (sources d2, e2, e3, e4, e5, e10). The faintest sources in table 4 are significantly mixed with background emission, such that their sizes and fluxes from Gaussian fitting are unreliable.

22

Source d2, although one of the brightest, is in a similar situation due to the strong background from IRS2. After by-eye inspection we consider the previously mentioned objects as point sources. Thus, we set their convolved size to one beam size, and their flux density equal to their peak intensity with an uncertainty equal to the noise per beam in the image.

For the sources for which we retrieved a valid Θ_{deconv}, their deconvolved solid angle Ω_{deconv} in steradian units is given by equation (2a). Therefore, their background-subtracted 2 cm brightness temperatures $T_{\mathrm{B,c}}$ and optical depths τ_{c} are as in equations (2b) and (2c):

$$\Omega_{\mathrm{deconv}} = \left(\frac{\pi}{4\ln 2}\right)(4.84 \times 10^{-6}\Theta_{\mathrm{deconv}})^2, \tag{2a}$$

$$T_{\mathrm{B,c}} = \left(\frac{c^2}{2k_{\mathrm{B}}\nu_{0,\mathrm{cm}}^2}\right)\left(\frac{S_{-\mathrm{bg}}}{\Omega_{\mathrm{deconv}}}\right), \tag{2b}$$

$$\tau_{\mathrm{c}} = \ln\left[\left(1 - \frac{T_{\mathrm{B,c}}}{T_{\mathrm{e}}}\right)^{-1}\right], \tag{2c}$$

where c is the speed of light, k_{B} is the Boltzmann constant, and T_e is the electron temperature. We find that assuming $T_{\mathrm{e}} = 7500\mathrm{K}$ as the typical temperature for an ionized plasma (Osterbrock & Ferland 2006) sources d2, e2, and e5 have brightness temperatures larger than T_{e}, so we do not determine continuum optical depths for them and we set their lower-limit τ_{c} values to unity. The rest of the sources are approximately optically thin. Optical depths are listed in table 4.

We also determined emission measures and electron densities from continuum parameters for these sources, using (see equation 10.35 of Wilson et al. 2009):

$$EM = 12.1433\tau_{\mathrm{c}}\left(\frac{\nu_{0,\mathrm{cm}}}{[\mathrm{GHz}]}\right)^{2.1}\left(\frac{T_{\mathrm{e}}}{[\mathrm{K}]}\right)^{1.35}, \tag{3a}$$

$$n_{\mathrm{e,c}} = \sqrt{EM/D}. \tag{3b}$$

where D is the deconvolved source diameter in pc. The calculated EM values are $\sim 10^7$ to 10^8 pc cm^{-6}, while electron densities are of order $n_{\mathrm{e,c}} \sim 10^4$ to 10^5 cm^{-3}, although three of them are lower limits.

Table 3. Derived sizes for sources in catalog B

Sources	$\theta_{\mathrm{maj}}/\theta_{\mathrm{min}}$ Θ_{conv} ['']	$N_{\mathrm{B,conv}}$	$\theta_{\mathrm{maj}}/\theta_{\mathrm{min}}$ Θ_{deconv} ['']	D [pc]
d2	$^{0.41}_{0.41}$ 0.41 ± 0.01	1.06 ± 0.01	$^{0.1}_{0.1}$ 0.1 ± 0.01	0.0026 ± 0.0001
d6	–	–	–	–
d7	$^{0.85}_{0.53}$ 0.67 ± 0.02	2.83 ± 0.20	$^{0.75}_{0.35}$ 0.51 ± 0.03	0.0135 ± 0.0009
e1	$^{1.04}_{1.03}$ 1.03 ± 0.04	6.69 ± 0.55	$^{0.96}_{0.94}$ 0.95 ± 0.05	0.0250 ± 0.0012
e2	$^{0.56}_{0.47}$ 0.51 ± 0.01	1.65 ± 0.03	$^{0.40}_{0.24}$ 0.31 ± 0.01	0.0082 ± 0.0002
e3	$^{0.51}_{0.47}$ 0.49 ± 0.01	1.52 ± 0.03	$^{0.32}_{0.25}$ 0.29 ± 0.01	0.0075 ± 0.0002
e4	$^{0.43}_{0.42}$ 0.43 ± 0.01	1.14 ± 0.02	$^{0.17}_{0.13}$ 0.15 ± 0.01	0.0039 ± 0.0003
e5	$^{0.44}_{0.43}$ 0.43 ± 0.01	1.18 ± 0.01	$^{0.19}_{0.15}$ 0.17 ± 0.01	0.0044 ± 0.0001
e6	$^{1.55}_{1.46}$ 1.50 ± 0.05	14.12 ± 0.89	$^{1.50}_{1.40}$ 1.45 ± 0.05	0.0380 ± 0.0013
e8n	–	–	–	–
e8s	–	–	–	–
e9	$^{0.68}_{0.61}$ 0.64 ± 0.02	2.58 ± 0.15	$^{0.54}_{0.46}$ 0.50 ± 0.02	0.0132 ± 0.0006
e10	$^{0.45}_{0.43}$ 0.44 ± 0.01	1.23 ± 0.04	$^{0.21}_{0.17}$ 0.19 ± 0.02	0.0049 ± 0.0005
e12	–	–	–	–
e13	–	–	–	–
e14	–	–	–	–
e20	–	–	–	–
e21	–	–	–	–
e22	–	–	–	–
e23	–	–	–	–

NOTE— Observational parameters obtained from Gaussian fitting of the 2 cm sources. These are the convolved Θ_{conv} and deconvolved Θ_{deconv} FWHM sizes – with the corresponding major θ_{maj} and minor θ_{min} axis components as a super(sub)script –, the source convolved size in beam units $N_{\mathrm{B,conv}}$, and the derived diameter D.

The ten objects marked with dashes are the aforementioned weak point sources for which we set upper limits to their deconvolved sizes and physical diameters of $0.15''$ and 0.004 pc, respectively. This corresponds to the minimum sizes recovered in valid fits.

Table 4. Physical parameters from 2 cm continuum

Sources	$I_{\rm pk}$	S	$S_{\rm -bg}$	$\tau_{\rm c}$	EM	$n_{\rm e,c}$	$\log_{10}(L_{\rm c})$
	[mJy beam^{-1}]	[mJy]	[mJy]		[10^8 pc cm^{-6}]	[10^5 cm^{-3}]	[s^{-1}]
d2^a	19.50 ± 1.00	19.50 ± 1.00	14.73 ± 1.00	> 1.0	> 4.84	> 4.30	> 46.01
d6	0.26 ± 0.05	0.26 ± 0.05	0.23 ± 0.07	–	–	–	–
d7	0.43 ± 0.02	1.22 ± 0.08	0.99 ± 0.16	< 0.01	0.02	0.11 ± 0.01	44.96 ± 0.11
e1	26.90 ± 1.60	180.00 ± 12.00	178.10 ± 12.01	0.19	0.94 ± 0.12	0.61 ± 0.04	47.25 ± 0.07
e2^a	108.00 ± 1.20	178.20 ± 3.00	177.78 ± 3.00	> 1.0	> 4.84	> 2.43	> 46.99
e3	15.44 ± 0.21	23.46 ± 0.48	23.11 ± 0.49	0.30	1.43 ± 0.10	1.39 ± 0.05	46.39 ± 0.04
e4	8.78 ± 0.10	9.99 ± 0.19	9.96 ± 0.20	0.54	2.62 ± 0.55	2.61 ± 0.29	46.08 ± 0.11
e5^a	26.27 ± 0.15	31.05 ± 0.29	31.17 ± 0.30	> 1.0	> 4.84	> 3.31	> 46.46
e6	4.50 ± 0.20	63.6 ± 3.0	63.00 ± 3.08	0.03	0.13 ± 0.02	0.19 ± 0.01	46.77 ± 0.05
e8n	2.68 ± 0.05	2.68 ± 0.05	2.55 ± 0.07	–	–	–	–
e8s	2.38 ± 0.05	2.38 ± 0.05	2.25 ± 0.07	–	–	–	–
e9	2.86 ± 0.12	7.39 ± 0.41	6.23 ± 0.43	0.02	0.11 ± 0.01	0.29 ± 0.02	45.76 ± 0.07
e10	2.02 ± 0.04	2.48 ± 0.09	2.47 ± 0.11	0.07	0.31 ± 0.06	0.80 ± 0.09	45.37 ± 0.12
e12	1.21 ± 0.05	1.21 ± 0.05	0.35 ± 0.07	–	–	–	–
e13	2.19 ± 0.05	2.19 ± 0.05	1.46 ± 0.07	–	–	–	–
e14	1.82 ± 0.05	1.82 ± 0.05	0.75 ± 0.07	–	–	–	–
e20	1.00 ± 0.05	1.00 ± 0.05	0.32 ± 0.07	–	–	–	–
e21	0.95 ± 0.05	0.95 ± 0.05	0.27 ± 0.07	–	–	–	–
e22	0.75 ± 0.05	0.75 ± 0.05	0.10 ± 0.07	–	–	–	–
e23	0.60 ± 0.05	0.60 ± 0.05	0.08 ± 0.07	–	–	–	–

NOTE— Values of peak intensity $I_{\rm pk}$, flux density S prior to background subtraction, flux density $S_{\rm -bg}$ after background subtraction, 2 cm optical depth $\tau_{\rm c}$, emission measure EM, continuum derived electron density $n_{\rm e,c}$, and Lyman photon rate $\log_{10}(L_{\rm c})$, as derived from the 2 cm continuum. ^{a} d2, e2 , and e5 have $T_{\rm B} > T_{\rm e} = 7500$ K, so we set their $\tau_{\rm c} > 1$. The ten objects marked with dashes $--$ are the weaker point sources mentioned in the text.

Further, we can use the electron densities and diameters of a given source to determine the amount of Lyman-continuum photons per second required for it to produce

3.1 2 *cm* Continuum

the observed emission, assuming ionization-recombination balance (Osterbrock & Ferland 2006):

$$L_{\mathrm{c}} = \frac{\pi}{6}\alpha_B n_{\mathrm{e,c}}^2 D^3, \tag{4}$$

where α_B is the Hydrogen recombination coefficient excluding transitions to the ground state, equal to 2×10^{-13} cm^{3}s^{-1}. All of the calculated values are shown in table 4.

3.2. Recombination Lines

Recombination line width has thermal and 'pressure' – collisional – contributions on top of the dynamical width. Pressure broadening increases as a steep power law of the principal quantum number (Gordon & Sorochenko 2002). Thus, for HC HIIs pressure broadening can be significant in cm RLs such as H77α, but is negligible (< 0.6 km s^{-1}) in the mm H30α line for all electronic densities $n_e < 10^7$ cm^{-3} (Galván-Madrid et al. 2012). In this work we perform a RL analysis similar to that presented in Keto et al. (2008) for brighter RL sources, whereby the thermal and dynamical contributions are determined from the H30α line, and are further used to determine the pressure contribution towards the H77α linewidth and the associated electron densities. Thanks to the sensitivity of ALMA, now we can perform such analysis in fainter HC HIIs.

We extracted the RL spectra of sources in catalog B using an aperture of radius equal to the 2σ level of each sources' convolved model Gaussian, that is, $R_{\mathrm{apert}} = 2 \times 0.42465\Theta_{\mathrm{conv}}$, which gives the flux within two standard deviations σ from the emission centroid. The spectra are then scaled up by a $1/0.95$ factor to account for the flux outside the aperture. Figure 8 shows plots of the RL spectra and Gaussian fits for those sources with at least one detection (catalogs $B - H77$ and $B - H30$ in table 1).

Eight objects were detected in H77α and eight were detected in H30α as well. Seven sources – d2, e1, e2, e3, e4, e5, e6 – were detected in both lines (catalog *B-H30-H77*). The Gaussian fitting and baseline removal was done using *PySpecKit* (Ginsburg &
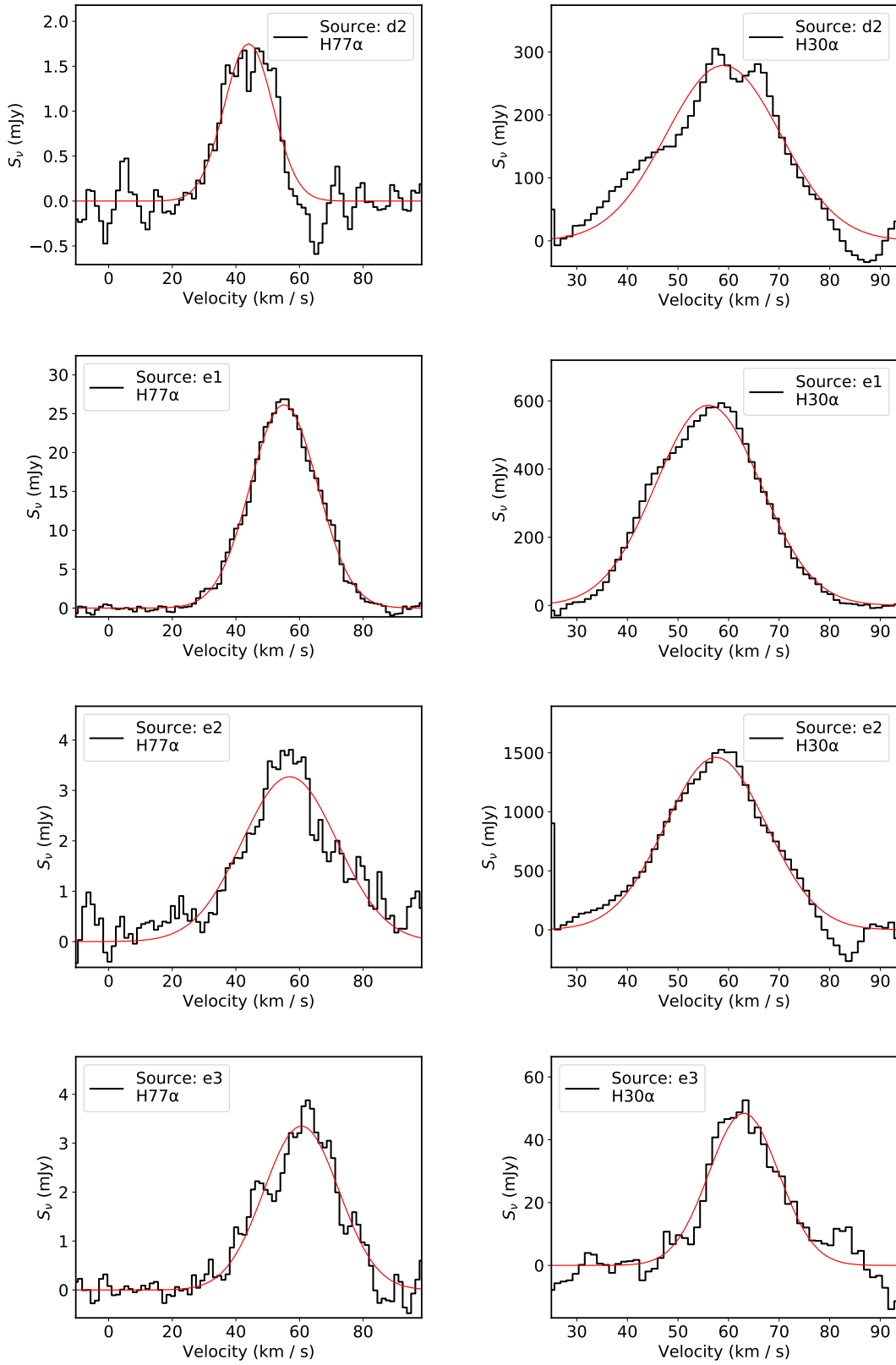
Figure 8. H77α (left) and H30α (right) RL spectra for sources d2, e1, e2, e3. Gaussian fits are indicated by the red line.
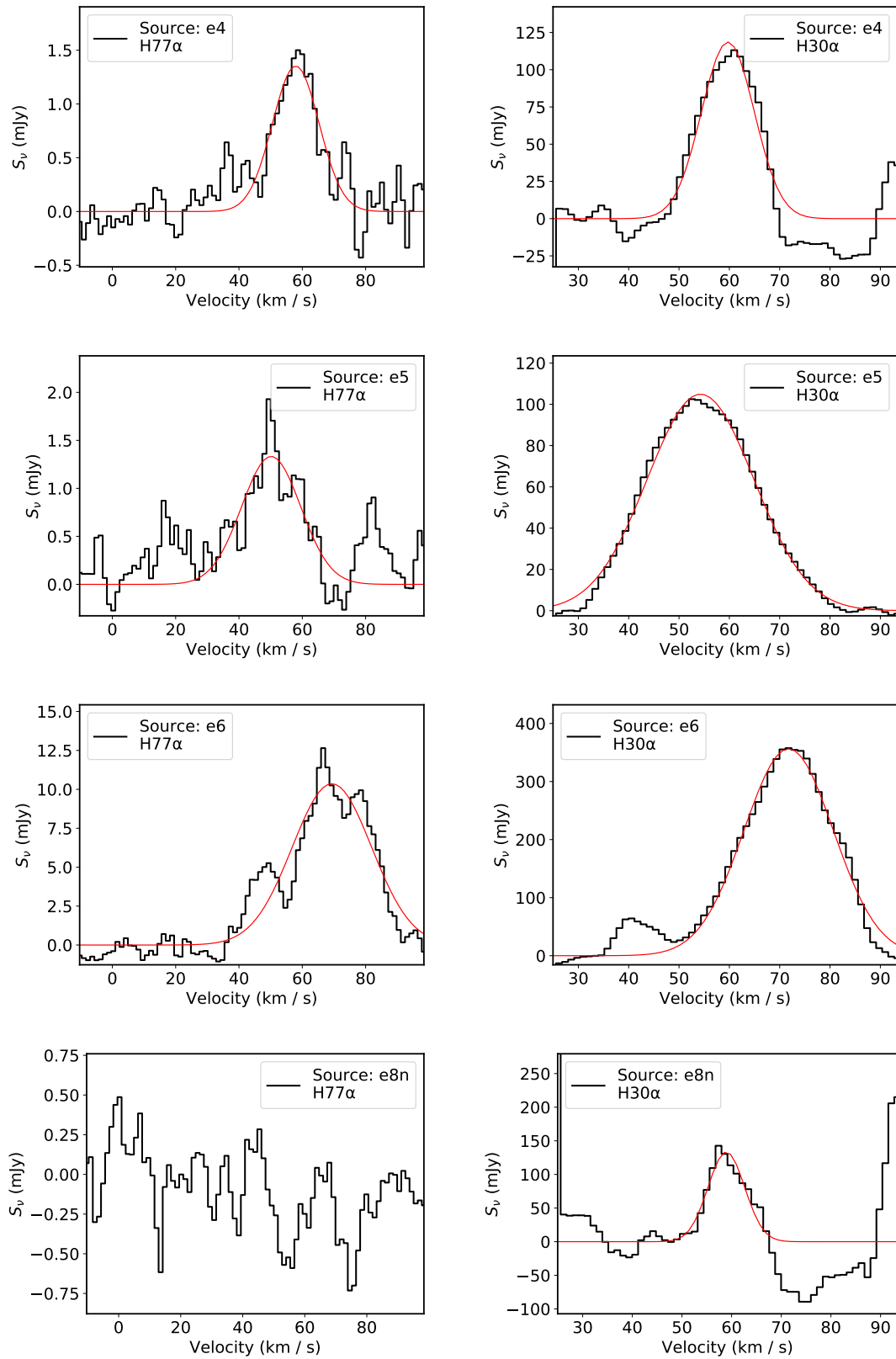
3.2 Recombination Lines

Figure 8. *contd.* H77α (left) and H30α (right) RL spectra for sources e4, e5, e6, and e8n. Gaussian fits are indicated by the red line.
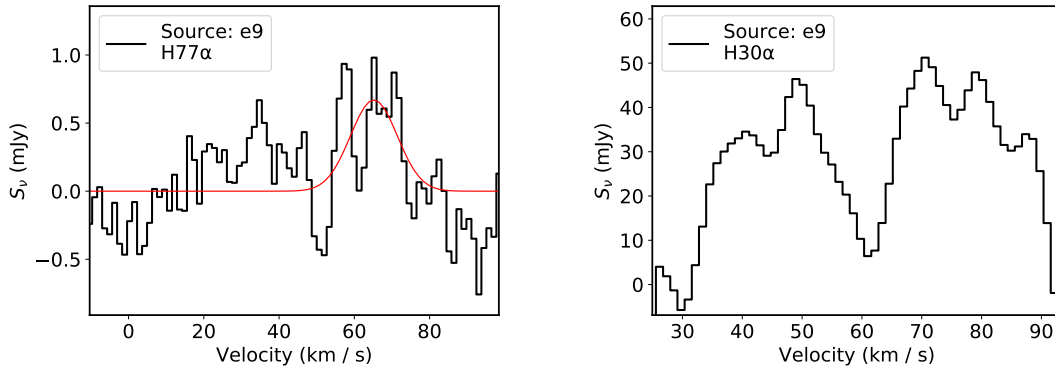
Figure 8. *contd.* H77α (left) and H30α (right) RL spectra for source e9. Gaussian fit is indicated by the red line.

Mirocha 2011). From the fitting results we derived the flux density, centroid velocity, and FWHM width of the RL emission as listed in table 5. Then we proceeded to derive the thermal Δv_{th}, dynamical Δv_{dy} and pressure Δv_{pr} broadening components following the prescriptions in Keto et al. (2008) and Galván-Madrid et al. (2012). Those results are summarized in table 6.

A few special considerations were made in some sources. For e8n H30α was detected but the intrinsically fainter H77α line was not. This is not unexpected. However, for e9 H77α was detected but H30α was not. After inspection of the images we concluded that in the H30α cube the source e9 lies at the position of a sidelobe caused by nearby bright emission, thus preventing detection. Sources d2, e4, and e8n have a negative bowl in their H30α spectra toward redshifted velocities caused by sidelobes of nearby bright emission. For source d2 these artefacts were partially alleviated by taking the spectrum from a single pixel at the peak rather than in an aperture. To be self-consistent the same was done for the H77α extraction in this source.

The contribution to line broadening due to the thermal velocity distribution of the gas particles has a Gaussian shape. Neglecting microturbulence, its FWHM is given by:

$$\Delta v_{\mathrm{th}} = \left(8 \ln 2 \frac{k_{\mathrm{B}} T_{\mathrm{e}}}{m_{\mathrm{H}}}\right)^{1/2}, \tag{5}$$

where m_{H} is the Hydrogen mass.

29

3.2 Recombination Lines

Table 5. Fits to recombination line spectra

Sources	H77α Peak Flux [mJy]	H77α Centroid [km s^{-1}]	H77α FWHM [km s^{-1}]	H30α Peak Flux [mJy]	H30α Centroid [km s^{-1}]	H30α FWHM [km s^{-1}]	$\Delta\nu_{77-30}$ [km s^{-1}]
d2	1.76 ± 0.18	44.00 ± 0.95	18.08 ± 2.23	278.88 ± 3.50	58.98 ± 0.16	26.67 ± 0.39	-14.97 ± 1.11
e1	26.16 ± 0.13	55.11 ± 0.06	24.87 ± 0.15	588.87 ± 2.75	56.01 ± 0.06	24.47 ± 0.13	-0.90 ± 0.12
e2	3.26 ± 0.10	56.84 ± 0.53	34.42 ± 1.25	1365.84 ± 3.11	58.31 ± 0.02	20.90 ± 0.06	-1.47 ± 0.55
e3	3.36 ± 0.13	60.59 ± 0.53	27.94 ± 1.24	48.50 ± 2.92	63.03 ± 0.48	16.24 ± 1.13	-2.44 ± 1.01
e4	1.35 ± 0.18	57.96 ± 1.09	16.95 ± 2.57	118.89 ± 3.52	59.70 ± 0.18	12.37 ± 0.42	-1.73 ± 1.27
e5	1.32 ± 0.14	50.31 ± 1.07	20.59 ± 2.51	105.28 ± 1.67	54.27 ± 0.20	25.14 ± 0.46	-3.96 ± 1.26
e6	10.54 ± 0.56	69.25 ± 0.80	30.89 ± 1.88	325.80 ± 10.34	71.65 ± 0.29	18.61 ± 0.69	-2.41 ± 1.09
e8n	–	–	–	105.52 ± 16.40	59.06 ± 0.53	6.92 ± 1.24	–
e9	0.67 ± 0.17	65.19 ± 1.87	14.68 ± 4.40	–	–	–	–

NOTE— Parameters derived from Gaussian fits to the H77α and H30α spectra, along with velocity centroid differences between the RLs. Source e8n lacks an H77α detection, and source e9 lacks an H30α detection. The d2 spectra was extracted from the central pixel rather than from an aperture due to image sidelobes in the H77α image caused by caused IRS2. This spectra could still be biased, so Δv_{77-30} could be artificially exaggerated for d2.

We exploit the fact that the H30α line is free of pressure broadening to infer the dynamical component from bulk motions such as outflows, winds, infall, or rotation. Assuming it is Gaussian, its FWHM is given by:

$$\Delta v_{\rm dy} = \sqrt{\Delta v_{\rm H30}^2 - \Delta v_{\rm th}^2}. \tag{6}$$

Considering that the profile of a pressure broadened line is a Lorentzian, whereas thermal and dynamic widths are taken as Gaussians, the H77α FWHM linewidth is given by a Voigt profile which can be expressed as (Keto et al. 2008):

$$\Delta v_{\rm H77} = 0.534\Delta v_{\rm pr} + (\Delta v_{\rm dy}^2 + \Delta v_{\rm th}^2 + 0.217\Delta v_{\rm pr}^2)^{1/2}. \tag{7}$$

Source d2 is anomalous in the sense that its H77α line appears to be narrower and blueshifted compared to H30α. We concluded that this could be due to the above

mentioned image artifacts, in particular sidelobes from the bright, nearby IRS2. Thus, in table 6 we do not report pressure broadening values for d2. The H30α line for sources e3 and e4 is narrower than $\Delta v_{\text{th}}(T_{\text{e}} = 7500K) = 18.52$ km s^{-1}, so for these we assume that there is no dynamical contribution to the broadening and derive the upper limit $T_{\text{e}} = T_{\text{e,upper}}$ necessary to account for their H30α linewidth. The resulting temperatures, listed in table 6, are still consistent with fully ionized gas, but indeed lower than the typically assumed value. The difference of the H77α and H30α linewidths for e5 is consistent with zero within 2σ. Then, for e5 we obtain an upper limit to the pressure broadening Δv_{pr} and electron density n_e using equations 7 and 8, and then substituting Δv_{H77} by $\Delta v_{\text{H30}} + \sigma_{\Delta v_{\text{H77}}}$ and $\Delta v_{\text{dy}}^2 + \Delta v_{\text{th}}^2$ by $(\Delta v_{\text{H30}} - \sigma_{\Delta v_{\text{H30}}})^2$.

Table 6. Broadening components and electron densities

Sources	Δv_{th} [km/s]	Δv_{dy} [km/s]	Δv_{pr} [km/s]	T_{e} [K]	$n_{\text{e,RL}}$ [10^5 cm^{-3}]
d2[a]	18.52	19.20	–	7500	–
e1	18.52	16.00	0.73 ± 0.36	7500	0.13 ± 0.06
e2[a]	18.52	9.68	21.18 ± 1.70	7500	3.62 ± 0.29
e3[b]	16.24	0.00	18.06 ± 2.13	5767	3.08 ± 0.36
e4[b]	12.37	0.00	7.64 ± 3.92	3345	1.31 ± 0.67
e5[a,c]	18.52	16.99	≤ 5.34	7500	≤ 0.913
e6	18.52	1.84	19.18 ± 2.69	7500	3.28 ± 0.46

NOTE—[a]: d2 does not have a derived Δv_{pr} nor $n_{\text{e,RL}}$ since its $\Delta v_{\text{H30}} > \Delta v_{\text{H77}}$. [b]: e3 and e4 have derived n_{e} using upper limit $T_{\text{e,upper}}$ found from assuming H30α width is entirely thermal ($\Delta v_{\text{dy}} = 0$). [c]: for e5 derived Δv_{pr} and n_{e} are upper limits as described in the text.

For sources e1, e2, e3, e4, e5, and e6 we calculate electron densities $n_{\text{e,RL}}$ from the derived pressure broadening components via equation (A.4) of Galván-Madrid et al. (2012),

$$n_{\text{e,RL}} = \Delta v_{\text{pr}} \Big(\frac{8.2\nu_{0,\text{H77}}^2}{c}\Big)\Big(\frac{n+1}{100}\Big)^{-4.5}\Big(1 + \frac{2.25\Delta n}{n+1}\Big)^{-1}, \tag{8}$$

3.2 Recombination Lines

where n is the quantum number and $\Delta n = 1$ for α transitions. The electron densities obtained from this RL analysis are $n_{\rm e,RL} \sim 10^4$ to 10^5 cm^{-3} as shown in table 6.

More information on the internal kinematics of the ionized gas can be extracted from the RL velocity centroids. Given that the H30α line traces on average higher densities than H77α, and under the assumption of a density profile decreasing with increasing radius, a blue- or redshifted H77α centroid with respect to H30α can be interpreted as outflowing or inflowing ionized gas, respectively (e.g., Keto et al. 2008). From table 5 it is seen that the nominal centroid values for H77α are *all blueshifted* with respect to H30α. The velocity differences Δv_{77-30} between the H77α and H30α centroids range from $\Delta v_{77-30} \approx -1$ to -4 km s^{-1} for all sources except for d2, which we deem to be artificially exaggerated (see above). Our main conclusion from this analysis is that the bulk of ionized gas at beam scales (~ 0.01 pc) in all these HC HIIs seems to be flowing outwards, not inwards. This could suggest that accretion has mostly ceased within our sample.

4.   Physical Properties of the HII Regions

Interestingly, the n_e and EM values we find through either or both methods are significantly smaller than those often-quoted for HCHIIs ($n_e \geq 10^6$ cm^{-3}, $EM \geq 10^{10}$ cm^{-6} pc, Kurtz 2005). The source diameters, however, are all in the range $D \sim 10^{-3}$ to 10^{-2} pc, which clearly puts them in the HC HII category.

We now show that our values are consistent with an extrapolation of UC HIIs to smaller sizes. Figure 9 shows n_e versus D for our sources along with the relations previously found in the literature for surveys of compact and UC HII regions at high angular resolution (Garay et al. 1993; Garay & Lizano 1999; Kim & Koo 2001). We find that our objects do follow these relations. Although radio surveys of UC HIIs can be considered to be comprehensive, HC HIIs are more difficult to detect, and it appears that most of them exist in crowded environments such as W51 A (Ginsburg et al. 2020). It is possible that previous detailed characterizations of HC HIIs are biased toward landmark objects, which happen to be relatively isolated and satisfy more specific selection criteria, such as also being *hyperdense* ($n_e > 10^6$ cm^{-3}) or having broad (FWHM > 50 km s^{-1}) millimeter RLs (e.g., Sewilo et al. 2004; Keto et al. 2008; Sánchez-Monge et al. 2011).

More can be learned from the determination of the spectral type of the stars ionizing our HII regions. The ionizing photon rates are shown in table 4 and figure 10. Only 2 (e1 and e2) out of 10 sources have measurements or lower limits above the threshold between O-type and B-type ZAMS stars $L_c \approx 10^{47}$ s^{-1} (Panagia 1973). e6 is close at $L_c \approx 46.8$ s^{-1}, and formally the lower limits for d2 and e5 could be above this threshold too. Therefore, 5 to 8 out of 10 sources are ionized by early B-type stars, not O-type stars. There is also a hint of a positive correlation between L_c and D that could be further explored with larger samples.
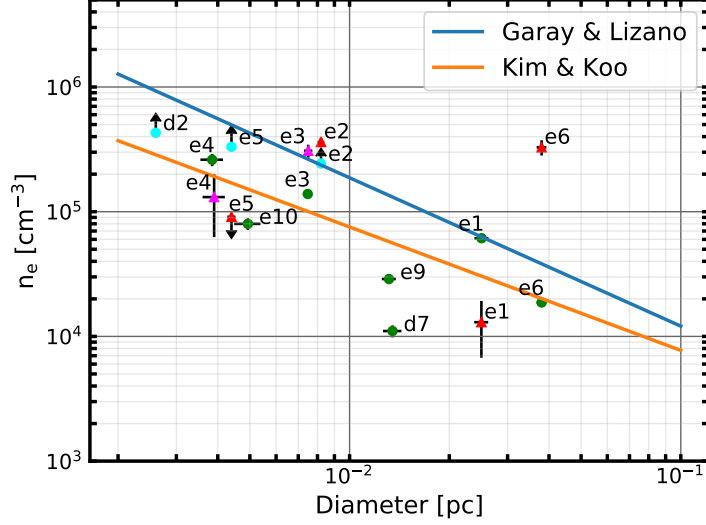
Figure 9. n_e vs D for sources in catalog B with a valid diameter measurement. *Triangles* correspond to RL-derived densities, color coded in *red* for those calculated with $T_e = 7500$ K and *magenta* for those calculated with a $T_e = T_{e,upper}$. *Circles* correspond to continuum-derived values, color coded in *green* for optically thin sources, and *cyan* for optically thick sources assuming $\tau_c = 1$. Arrows indicate lower or upper limits. The *blue* and *orange* lines show the relations previously derived by Garay & Lizano (1999), $n_e = 780 \times D^{-1.19}$, and Kim & Koo (2001), $n_e = 790 \times D^{-0.99}$.
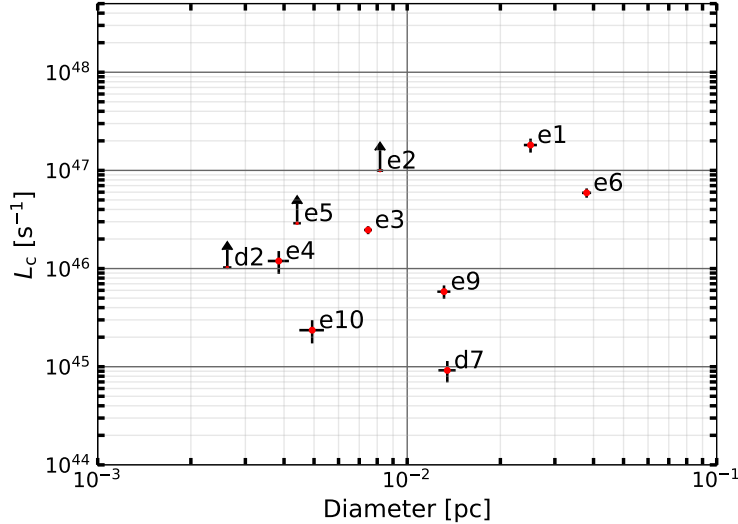
Figure 10. L_c *vs* D for sources in catalog B with a valid diameter measurement. The arrows represent lower limits due to high optical depths.

5. Molecular Lines Toward Radio Continuum Sources

Using the ALMA data release from Ginsburg et al. (2017), we investigate the dense molecular gas content of our HC HII region sample (catalog B). Table 7 lists the physical properties of the available lines of formaldehyde $H_2CO(3_{0,3} - 2_{0,2})$, $H_2CO(3_{2,1} - 2_{2,0})$, and of sulfur monoxide $SO(6_5 - 5_4)$. The critical densities ($n_{cr} \sim 10^6$ cm^{-3}) and upper-level energies ($E_U = 21$ to 68 K) are similar among the three lines, but the chemistry of H_2CO and SO is expected to be different: H_2CO is considered a standard tracer of dense gas in molecular clouds (e.g., Henkel et al. 1983; Ginsburg et al. 2016), whereas SO and other sulphur-bearing molecules are thought to trace shocked regions (Pineau des Forets et al. 1993). At the resolution probed by our observations, the spectra from these possibly shocked regions traced by SO could be a combination of emission from gas in the inner hot molecular core (HMC) and gas further away from the stars in the line of sight (e.g., Guzmán et al. 2018).

Table 7. Molecular Line Properties

Molecule	E_l	E_u	A_{ul}	B_{ul}	n_{crit}^{100K}
	[K]	[K]	$[10^{-4}s^{-1}]$	$[10^{-11}cm^3s^{-1}]$	$[10^6cm^{-3}]$
$H_2CO(3_{0,3} - 2_{0,2})$	10.5	21.0	2.8	8.4	3.4
$H_2CO(3_{2,1} - 2_{2,0})$	57.6	68.1	1.6	4.9	3.2
$SO(6_5 - 5_4)$	24.4	35.0	1.3	5.8	2.3

NOTE—Lower and upper level energies for each molecular transition, Einstein coefficients, and critical densities at 100 K.

We extracted the molecular-line spectra on catalog B over the same apertures as for the RLs, and have taken two approaches towards their analysis. First, in §5.1 we compare the detected molecular line profiles with respect to each other. Second, in §5.2 we compare the velocities of the molecular spectral features to the stellar velocities probed by the H30α centroid. Thus, this second analysis is limited to catalog B-$H30$ (see figure 12).

5.1. Comparison Between Molecular Lines

Figure 11 shows the velocity-integrated intensity (moment 0) maps for the three molecular lines. As is known, (e.g., Ginsburg et al. 2017), the total emission is dominated by IRS2 and the e2/e8 subcluster. However, it is seen that the compact sources in catalog B tend to be associated with structures of molecular gas. Both H_2CO lines are detected for 20/20 sources and the SO line is detected in 14/20 sources.

The molecular spectral profiles of 8 objects could not be analyzed because most of the fainter sources (d6, d7, e12, e20, e21, e23, e23) and source e6 were affected by image sidelobes from the brightest emission in the map. These uncharacterized sources are shown in figure 14 in the appendix. For the sources that were characterized, figure 12 shows the molecular spectra for sources with H30α detection (catalog *B-H30*, except e6), which tend to be among the brightest with peak molecular fluxes up to ~ 1 Jy. The complementary figure 13 in the appendix shows the molecular spectra for the analyzed sources without H30α.

The molecular profiles have a variety of shapes, but all of them have FWHM widths from ~ 5 to 20 km s^{-1}, clearly signaling bulk motions far larger than the thermal width < 0.5 km s^{-1}. These bulk motions could be due to expansion, outflow, infall, and/or rotation. In principle, some of these motions could be figured out from the shape of the molecular spectra under reasonable assumptions of the temperature, density, and velocity profiles (e.g., Myers et al. 1996).

We qualitatively group the molecular spectra of the 12 objects in figures 12 and 13 in three categories based on their profiles: 1) a single, almost symmetrical emission component, 2) the presence of significant asymmetries or multiple emission components, and 3) the presence of a prominent absorption component, often accompanied by emission features. The first group is consistent with molecular gas that is optically thin. The second group has asymmetries which we label as "blue-" or "red-peaked", and could also have dips in the profile. In the third group we only have source e2 with an inverse P-Cygni profile. In this source the continuum background from the hot

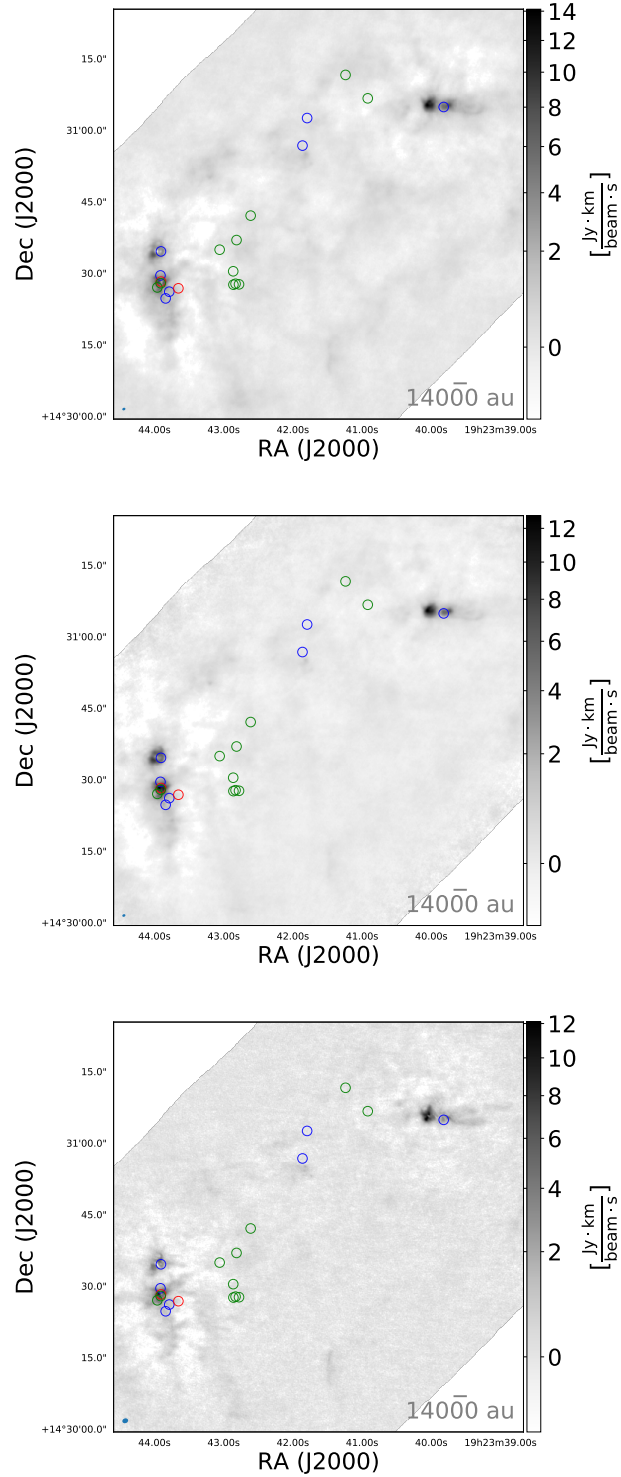**Figure 11.** Velocity-integrated (moment 0) images of $H_2CO(3_{0,3} - 2_{0,2})$ (top, $\sigma_{rms} \sim 0.15$ Jy beam^{-1} km s^{-1}), $H_2CO(3_{2,1} - 2_{2,0})$ (middle, $\sigma_{rms} \sim 0.10$ Jy beam^{-1} km s^{-1}), and SO (bottom, $\sigma_{rms} \sim 0.14$ Jy beam^{-1} km s^{-1}). The color stretch is square-root from $-3\sigma_{rms}$ to the absolute maximum in the respective image. Velocity integration was performed from 35 km s^{-1} to 75 km s^{-1}. Circles mark the position of 2 cm sources as labeled in figure 7.

37

5.1 Comparison Between Molecular Lines

HC HII is relevant, which results in the observed prominent absorption. Finally, regardless of category, in some sources we additionally identify high-velocity line wings, which indicate the presence of faster outflows.

Our interpretation of blue-peaked profiles follows the widely used models of inside-out collapse with radially decreasing temperature and velocity profiles (e.g., Shu 1977; Myers et al. 1996; Churchwell et al. 2010), in which the decreased brightness at redshifted velocities is caused by self-absorption from the cooler, outer layers of the object in the observer's side. Hence, we denote those sources with blue-peaked profiles as *infall* candidates. Red-peaked profiles have been described in YSO surveys (e.g., Mardones et al. 1997) and have been associated with bulk expansion of molecular envelopes (e.g., Thompson & White 2004; Velusamy et al. 2008). Therefore, we denote such sources as *expansion* candidates. The inverse P-Cygni profile in e2 is a signature of infall. We do not consider more complex kinematics as alternate mechanisms for producing profile asymmetries, such as bipolar outflows, rotation, or multiplicity (e.g., Cabrit & Bertout 1986; Izquierdo et al. 2018).

Table 8 summarizes our assessment of the molecular profiles for the 12 sources in catalog B whose spectra was characterized. We now comment on the individual line profiles summarized in table 8:

- d2 lines are single-peaked. The H_2CO lines are slightly red-peaked and SO is symmetrical. There is a blue high-velocity wing in all three lines. Expansion candidate.

- e1 is red-peaked in the $H_2CO(3_{0,3} - 2_{0,2})$ and SO lines. The SO also has a broad, redshifted wing extending up to ~ 40 km s^{-1} from the absorption dip, suggesting the presence of a fast outflow. Expansion candidate.

- e2 has two emission peaks on each side of the prominent absorption peak in all spectra. The line profiles are similar to inverse P-Cygni. Infall candidate.

- e3 is blue-peaked in all spectra. The red emission shoulder in $H_2CO(3_{0,3} - 2_{0,2})$ becomes a secondary peak in $H_2CO(3_{2,1} - 2_{2,0})$ and SO. A second, fainter shoulder is also seen in H_2CO lines. Infall candidate.

- e4 is symmetrical in $H_2CO(3_{2,1} - 2_{2,0})$ and blue-peaked with a prominent red-shifted shoulder in $H_2CO(3_{0,3} - 2_{0,2})$ and SO. Blue- and redshifted wings are seen in all lines. Infall candidate.

- e5 has a central dip reaching zero flux in the H_2CO lines and presents absorption in SO. We tentatively interpret these as due to an expanding shell with some absorption against the background continuum. The main peak is toward the red in $H_2CO(3_{2,1} - 2_{2,0})$ and SO, suggesting asymmetries in the shell. Expansion candidate.

- e8n spectra are red-peaked with a prominent blue shoulder in all lines. SO shows self-absorption at velocities slightly blueshifted from the main peak. Expansion candidate.

- The spectra of e8s are very similar to its neighbour e8n. They could be mixed. Expansion candidate.

- e9 is red-peaked in all lines. The faint apparent absorption at ≈ 50 km s^{-1} in both H_2CO lines is a sidelobe artifact. Expansion candidate.

- The spectra in e10 are very broad. $H_2CO(3_{0,3} - 2_{0,2})$ appears to have several dips, $H_2CO(3_{2,1} - 2_{2,0})$ is red-peaked, and SO appears almost symmetrical with prominent shoulders. In all lines the main emission extends from ~ 40 to 80 km s^{-1}. We consider e10 as a fast expansion candidate.

- e13 has faint and narrow (width < 10 km s^{-1}) spectra. The lines are slightly red-peaked. Expansion candidate.

- The faint lines in e14 appear multiple-peaked in H_2CO. $H_2CO(3_{2,1} - 2_{2,0})$ and SO are red-peaked. Expansion candidate.

In summary, we have 3 out of 12 sources (e2, e3, e4) whose molecular envelope appears to have bulk infall motions, whereas 9 out of 12 sources (d2, e1, e5, e8n, e8s, e9, e10, e13, e14) appear to be in bulk expansion. Four sources (1 with infall and 3 with expansion) have high-velocity line wings signaling additional, faster outflows. The 3 infall candiates are in the e2/e8 subcluster, which is expected as this is one the most active sites of current star formation (e.g., Goddi et al. 2016; Ginsburg et al. 2017).

5.2 Comparison to stellar velocities

Table 8. Inferred molecular kinematics

Sources	$H_2CO(3_{0,3} - 2_{0,2})$	$H_2CO(3_{2,1} - 2_{2,0})$	$SO(6_5 - 5_4)$	Candidate
d2	Red+BW	Red+BW	Sym+BW	*Exp*
e1	Red	Sym	Red+RW	*Exp*
e2	inv. P-Cyg	inv. P-Cyg	inv. P-Cyg	*Inf*
e3	Blue	Blue	Blue	*Inf*
e4	Blue+BRW	Sym+BRW	Blue+BRW	*Inf*
e5	Sym	Red	Red	*Exp*
e8n	Red	Red	Red	*Exp*
e8s	Red	Red	Red	*Exp*
e9	Red	Red	Red	*Exp*
e10	Sym+BRW	Red+BRW	Sym+BRW	*Exp*
e13	Sym	Red	Red	*Exp*
e14	Sym	Red	Red	*Exp*

NOTE—2nd, 3rd, 4th columns: Red/Blue: line profile with *red* or *blue* absolute peak, respectively. Sym: symmetric profile. Abs: prominent absorption feature(s). inv. P-Cyg: inverse P-Cygni profile. +RW/+BW: additional red/blue high-velocity wings in line profile. 5th column: *Exp* for expansion candidates, *Inf* for infall candidates.

5.2. Comparison to stellar velocities

Given that the material closest to the massive (proto)stars within HC HIIs is ionized, and that the H30α is a better kinematical tracer of the denser ionized gas compared to lower-frequency RLs, it is reasonable to take the H30α velocity centroid as a proxy for the stellar velocity (e.g., Keto et al. 2008; Zhang et al. 2019). A comparison of the molecular spectra with the H30α velocity for catalog *B-H30* (except e6, see above) is shown in figure 12. Large velocity differences indicate significant offsets between the "mean" – bulk – motions of the respective molecular component and the HC HII region.

Four out of seven sources have the molecular profile – either the central peak or the main absorption component – aligned within a few km s^{-1} with the H30α velocity

centroid: d2, e1, e5, e8n. Thus, these sources have their molecular kinematics almost symmetrically centered around the stellar velocity. However, for the other three sources (e2, e3, e4) the H30α RL is offset and redshifted $\gtrsim 5$ km s^{-1} from the main molecular peak. This can be interpreted in two ways: either the star has significant motions with respect to its dense molecular core, or the H30α emission does not appropriately trace the stellar velocity. We tentatively discard the latter because the H30α profiles are mostly optically thin Gaussians. However, the former explanation suggests that the stellar motions of these sources share a common offset with respect to their parent cores, which is plausible given the fact that e2, e3, and e4 form part of the same cluster. Goddi et al. (2016) infers systemic velocities for the e2 and e8n cores of 57.4 and 59.9 km s^{-1}, respectively. These velocities are coincident with the main spectral feature of both objects through all line transitions, which seem to corroborate our interpretation.

Such velocity offsets between molecular and ionized tracers have been observed in other UC and HC HIIs (e.g., Liu et al. 2012; Klaassen et al. 2018). They are expected due to the complex interaction between these gas phases in a dynamical scenario for massive star formation (e.g., Peters et al. 2010a,b).

Finally, for all sources the SO line is systematically blueshifted with respect to the H$_2$CO lines. As mentioned above, a plausible explanation is that SO is tracing a shocked layer more external than H$_2$CO, with kinematics more often dominated by outflow motions. Also, the SO profiles tend to be more asymmetric, suggesting larger optical depths.
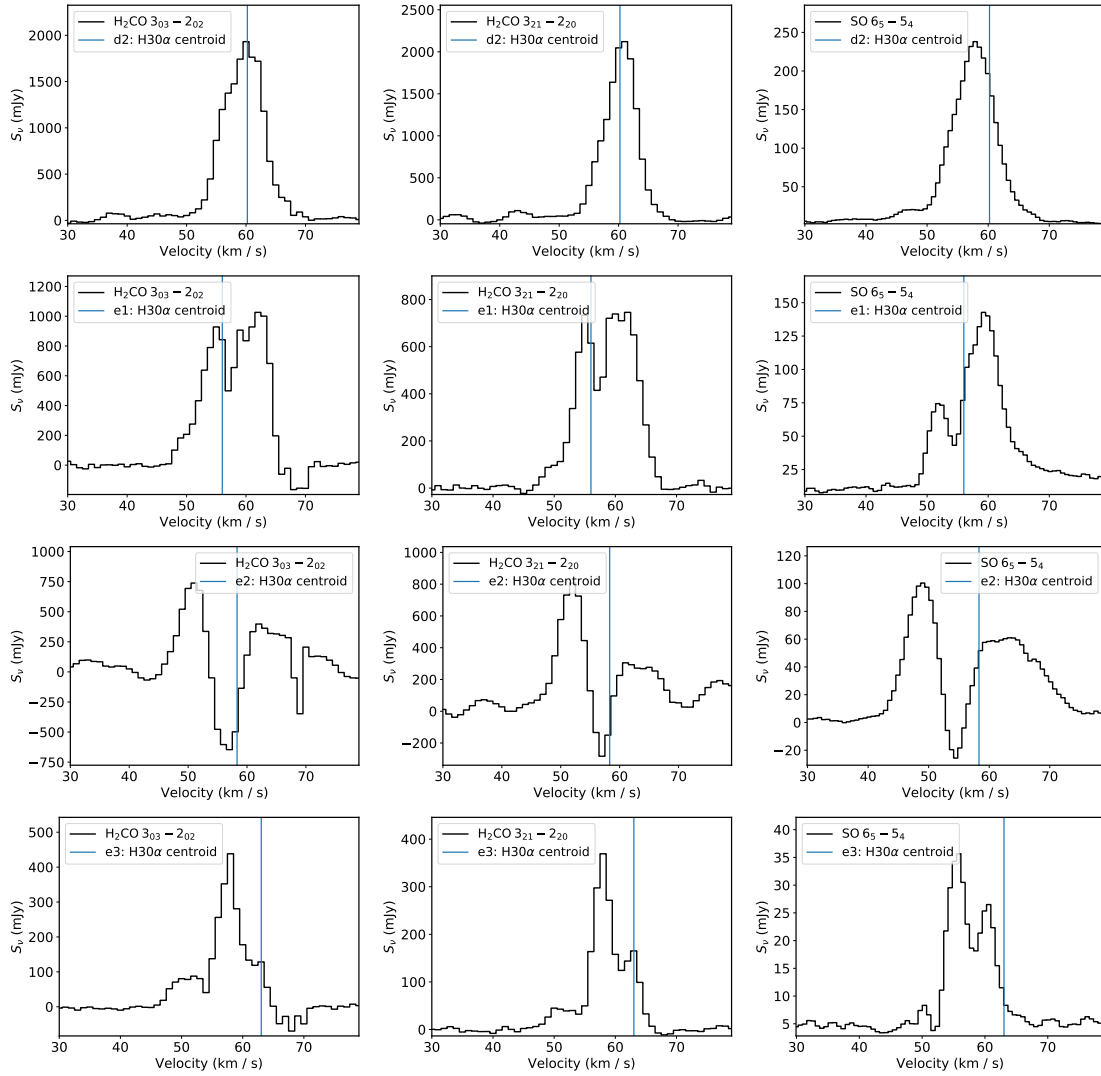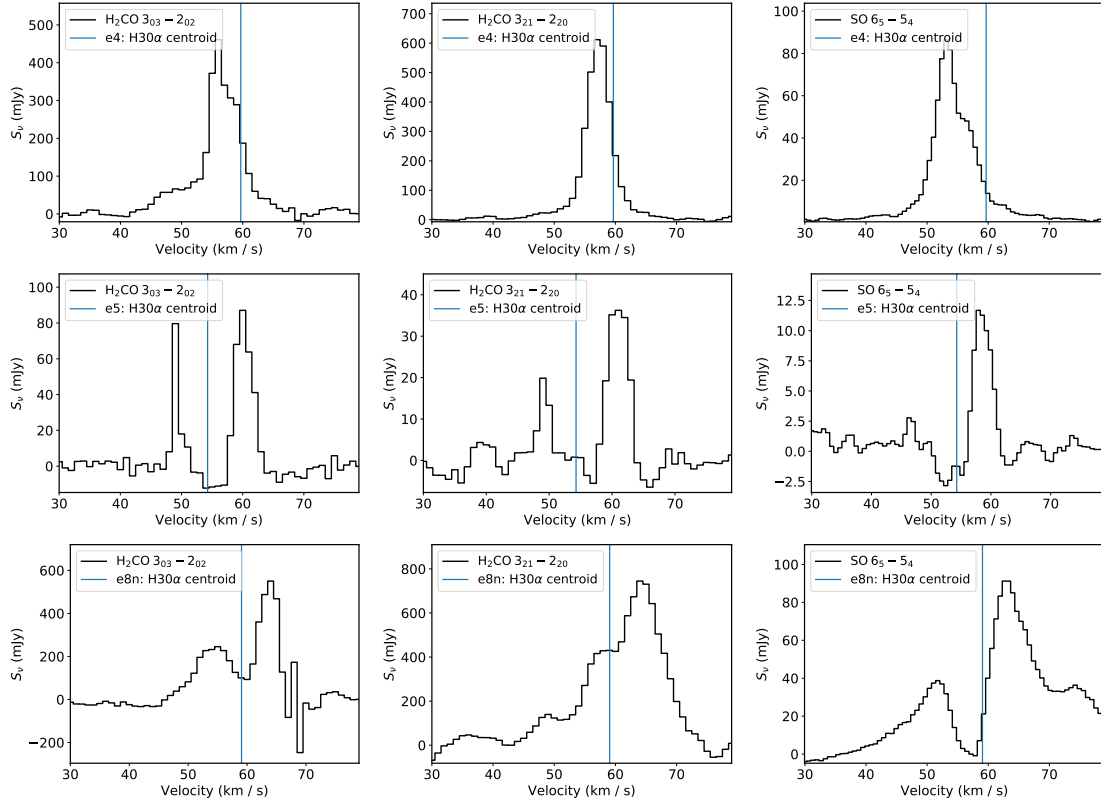
5.2 Comparison to stellar velocities

Figure 12. Spectral profiles of the molecular transitions $H_2CO(3_{0,3} - 2_{0,2})$ – left –, $H_2CO(3_{2,1} - 2_{2,0})$ – middle –, $SO(6_5 - 5_4)$ – right – for sources d2, e1, e2, and e3 from catalog *B-H30*. The H30α velocity centroid – proxy for the stellar velocity – is marked with a blue line.

Figure 12. *contd.* Spectral profiles of the molecular transitions $H_2CO(3_{0,3} - 2_{0,2})$ – left –, $H_2CO(3_{2,1} - 2_{2,0})$ – middle –, $SO(6_5 - 5_4)$ – right – for sources e4, e5, and e8n from catalog *B-H30*. The H30α velocity centroid – proxy for the stellar velocity – is marked with a blue line.

6. Discussion

6.1. The nature of hypercompact HII regions in W51 A

We found bulk *outward* motions in the ionized gas for *all* the 7 sources for which we could infer their kinematics from a comparison of the H30α and H77α RLs. We also found that *all* 20 HC HIIs in the common ALMA+VLA field are associated with dense molecular gas, and determined that their molecular-gas kinematics tend to favor outward motions (9/12) too. For the subsample of H30α RL sources we see signatures of molecular infall about as often as outflow (3/7).

We conclude that, in our sample, accretion onto the protostar(s) has halted for the most part, although higher angular resolution observations are needed to resolve any remaining accretion flows (e.g., Goddi et al. 2018).

We derived electron densities from the RL analysis, as well as emission measures and electron densities from the 2 cm continuum.

Through both methods we find that the electron densities are larger than those of UC HII regions, yet smaller than typically defined for HC HIIs (Kurtz 2005). Interestingly, we find that our sources follow the n_e vs D inverse relations previously found by Garay & Lizano (1999) and Kim & Koo (2001) for samples of compact and UC HII regions. Our interpretation is that we are characterizing a population of HC HII regions that are more common than landmark objects. This, combined with the previously discussed expansion kinematics in ionized gas, suggests that the majority of these HC HIIs are essentially smaller versions of expanding UC and compact HII regions.

Our determination of the early B spectral type for the stars within our sources supports the aforementioned interpretation, and is also consistent with the initial mass function that ionizing stars in the ZAMS would be expected to follow.

We also note that none of our sources fall in the category of "broad recombination line" HII regions (e.g., Sewilo et al. 2004; De Pree et al. 2004), which could be truly different objects where accretion is still ongoing.

44

We speculate that there could be two different physical objects denominated as "hypercompact" HII regions due to their $D \sim 10^{-3} - 10^{-2}$ pc diameters: i) the most common would be mostly B-type stars (although some O-stars are expected) with little to no remaining accretion producing tiny HII regions that are mostly expanding (e.g., see discussion in Kurtz 2002). ii) special objects with extremely high densities and large (sub)mm recombination linewidths. These could be the ionized accretion flows expected to occur in the formation of stars more massive than about 20 to 30 $M_\odot$ (Keto 2007; Peters et al. 2010a). Under the previously described scenario, not all HC HIIs would evolve to become UC HIIs ionized by ZAMS O-type stars. It would depend on the local gas reservoir and final accretion history (Peters et al. 2010b; Galván-Madrid et al. 2011).

6.2.   Comparison to previous studies

The compact radio continuum objects e1 and e2 were identified by Scott (1978). Higher resolution observations at 3.6 and 1.3 cm by Gaume et al. (1993) found d2, e3, e4, and e5. Those authors derived electron densities and emission measures in agreement with our values in most cases ($n_\mathrm{e} \sim 10^4$ to 10^6 cm^{-3}, $EM \sim 10^7$ to 10^9 pc cm^{-6}). Source e6 was first observed by Mehringer (1994), who derived lower limit densities and emission measures for e1, e2, and e6 $n_\mathrm{e} \sim 10^3$ to 10^6 cm^{-3}, $EM \sim 10^6$ pc·cm^{-6}, which are lower but still comparable with our calculations. Additionally, for e2 Keto et al. (2008) found $n_\mathrm{e} \sim 2 \times 10^6$ cm^{-3} derived from H53α and H66α, which is about an order of magnitude larger than our H77α derived value (see table 6). This difference can be explained if the RLs are partially optically-thick (the continuum of e2 has $\tau_\mathrm{c} \gg 1$) and the lower quantum numbers are more sensitive to denser gas, or by our higher S/N data. Source e8n was first seen at 1.3 cm by Zhang & Ho (1997), but not characterized.

Earlier references found evidence for molecular infall toward e2 (e.g., Zhang & Ho 1997). Later it was found that e2 is resolved into three (sub)mm cores e2-E, e2-W, and e2-NW (Shi et al. 2010b). e2-W corresponds to the cm e2 HC HII region.

6.2 Comparison to previous studies

Accretion activity seems to be concentrated in e2-E (Shi et al. 2010a; Goddi et al. 2016), and the separation between the sources is $1''$.

7. Conclusions

• We derived deconvolved diameters for the 2 cm continuum of 10/20 sources in catalog B (d2, d7, e1, e2, e3, e4, e5, e6, e9, e10), and found them to be within the regime of HC HII regions: $D \sim 10^{-3}$ to 10^{-2} pc.

• We calculated the electron densities of these HC HIIs, finding $n_{\rm e,c} \sim 10^4$ to 10^5 cm^{-3}. The respective emission measures are $EM \sim 10^7$ to 10^8 pc cm^{-6}.

• We analyzed the RLs of the 7 objects in catalog B-$H30$-$H77$ (d2, e1, e2, e3, e4, e5, e6) and calculated electron densities also of the order of $n_{\rm e,RL} \sim 10^4$ to 10^5 cm^{-3}.

• The electron densities obtained from both methods are comparable to each other and significantly smaller than often defined for HC HII regions ($n_{\rm e} \geq 10^6$ cm^{-3}, $EM \geq 10^{10}$ cm^{-6} pc). However, they follow the relation between n_e and D previously found in the literature for samples UC and compact HII regions.

• We calculated the Lyman continuum photon rates and found that these HC HIIs tend to be ionized by early B-type stars, not O-type stars.

• From the analysis of the RL velocity centroids, we found that the bulk of the ionized gas in the 7 objects in catalog B-$H30$-$H77$ is going outwards, suggesting that accretion has mostly ceased within our sample.

• We found that all the 20 cm continuum sources in catalog B have detections in H_2CO, and 14 of them in SO. This suggests that, at least in a clustered environment such as in W51 A, the HC HII stage is always associated with the presence of local, dense molecular gas.

• We could analyze the molecular line profiles for 12 of the 20 detections, finding that 9 of them have evidence of expansion motions, whereas only 3 of them have evidence of infall. The three infall candidates (e2, e3, and e4) belong to the same cluster.

• We could compare the velocity centroids of 7 of the 8 H30α detections to their respective molecular lines. Four sources (d2, e1, e5, e8n) show no significant offsets between the ionized and molecular components. For the other 3 (also e2, e3, and e4) the H30α line is redshifted, suggesting systematic relative motions between the star

cluster and their surrounding molecular material.

We have performed a thorough characterization of the HC HII population in W51 A, where *hypercompact* is defined as having a diameter smaller than 0.05 pc. We find that these HC HIIs behave as expected in some aspects (presence of dense molecular gas, infall and outflow molecular kinematics), but are surprising in some other (in most cases less dense than expected, purely outflows in ionized gas). The finding that they behave like smaller UC HIIs ionized by early B-type stars suggests that there could be two different types of very small HII regions: the more common one associated to the more abundant B-type stars, and a few truly *hyperdense* objects associated with O-type stars in a specific evolutionary stage.

REFERENCES

Aguirre, J. E., Ginsburg, A. G., Dunham, M. K., et al. 2011, ApJS, 192, 4

Brogan, C. L., Goss, W. M., Hunter, T. R., et al. 2013, ApJ, 771, 91

Cabrit, S., & Bertout, C. 1986, ApJ, 307, 313

Chou, J., Lin, D.-B., Lin, C.-H., & Li, H.-J. 2013, 2013 Proceedings of the International Symposium on Antennas and Propagation, 01, 276

Churchwell, E. 2002, ARA&A, 40, 27

Churchwell, E., Sievers, A., & Thum, C. 2010, A&A, 513, A9

Combes, F. 1991, ARA&A, 29, 195

Condon, J. J., & Ransom, S. M. 2016, Essential Radio Astronomy (Princeton University Press)

De Pree, C. G., Wilner, D. J., Mercer, A. J., et al. 2004, ApJ, 600, 286

De Pree, C. G., Peters, T., Mac Low, M. M., et al. 2014, ApJL, 781, L36

Galván-Madrid, R., Goddi, C., & Rodríguez, L. F. 2012, A&A, 547, L3

Galván-Madrid, R., Keto, E., Zhang, Q., et al. 2009, ApJ, 706, 1036

Galván-Madrid, R., Peters, T., Keto, E. R., et al. 2011, MNRAS, 416, 1033

Galván-Madrid, R., Liu, H. B., Zhang, Z. Y., et al. 2013, ApJ, 779, 121

Garay, G., & Lizano, S. 1999, PASP, 111, 1049

Garay, G., Rodriguez, L. F., Moran, J. M., & Churchwell, E. 1993, ApJ, 418, 368

Gardner, F. F., & Morimoto, M. 1968, Australian Journal of Physics, 21, 881

Gaume, R. A., Johnston, K. J., & Wilson, T. L. 1993, ApJ, 417, 645

Ginsburg, A., Bally, J., Battersby, C., et al. 2015, A&A, 573, A106

Ginsburg, A., & Mirocha, J. 2011, PySpecKit: Python Spectroscopic Toolkit, Astrophysics Source Code Library, ascl:1109.001

Ginsburg, A., Goss, W. M., Goddi, C., et al. 2016, A&A, 595, A27

Ginsburg, A., Goddi, C., Kruijssen, J. M. D., et al. 2017, ApJ, 842, 92

Ginsburg, A., Anderson, L. D., Dicker, S., et al. 2020, arXiv e-prints, arXiv:2004.09555

Goddi, C., Ginsburg, A., Maud, L., Zhang, Q., & Zapata, L. 2018, arXiv e-prints, arXiv:1805.05364

Goddi, C., Ginsburg, A., & Zhang, Q. 2016, A&A, 589, A44

Gordon, M. A., & Sorochenko, R. L., eds. 2002, Astrophysics and Space Science Library, Vol. 282, Radio Recombination Lines. Their Physics and Astronomical Applications

Guzmán, A. E., Guzmán, V. V., Garay, G., Bronfman, L., & Hechenleitner, F. 2018, ApJS, 236, 45

Guzmán, A. E., Garay, G., Rodríguez, L. F., et al. 2014, ApJ, 796, 117

Henkel, C., Wilson, T. L., Walmsley, C. M., & Pauls, T. 1983, A&A, 127, 388

Hoare, M. G., Kurtz, S. E., Lizano, S., Keto, E., & Hofner, P. 2007, Protostars and Planets V, 181

Hosokawa, T., Yorke, H. W., & Omukai, K. 2010, ApJ, 721, 478

Izquierdo, A. F., Galván-Madrid, R., Maud, L. T., et al. 2018, MNRAS, 478, 2505

Kang, M., Bieging, J. H., Povich, M. S., & Lee, Y. 2009, ApJ, 706, 83

Keto, E. 2003, ApJ, 599, 1196

—. 2007, ApJ, 666, 976

Keto, E., & Klaassen, P. 2008, ApJL, 678, L109

Keto, E., Zhang, Q., & Kurtz, S. 2008, ApJ, 672, 423

Kim, K.-T., & Koo, B.-C. 2001, ApJ, 549, 979

Klaassen, P. D., Johnston, K. G., Urquhart, J. S., et al. 2018, A&A, 611, A99

Kurtz, S. 2002, Astronomical Society of the Pacific Conference Series, Vol. 267, Ultracompact HII Regions, ed. P. Crowther, 81

Kurtz, S. 2005, in IAU Symposium, Vol. 227, Massive Star Birth: A Crossroads of Astrophysics, ed. R. Cesaroni, M. Felli, E. Churchwell, & M. Walmsley, 111

Kurtz, S., Churchwell, E., & Wood, D. O. S. 1994, ApJS, 91, 659

Liu, H. B., Jiménez-Serra, I., Ho, P. T. P., et al. 2012, ApJ, 756, 10

Lodro, M. 2016, Antennas and Wave Propagation

MacLeod, J. M., & Doherty, L. H. 1968, ApJ, 154, 833

Mardones, D., Myers, P. C., Tafalla, M., et al. 1997, in American Institute of Physics Conference Series, Vol. 393, American Institute of Physics Conference Series, ed. S. S. Holt & L. G. Mundy, 113

Martin, A. H. M. 1972, MNRAS, 157, 31

McMullin, J. P., Waters, B., Schiebel, D., Young, W., & Golap, K. 2007, in Astronomical Society of the Pacific Conference Series, Vol. 376, Astronomical Data Analysis Software and Systems XVI, ed. R. A. Shaw, F. Hill, & D. J. Bell, 127

Mehringer, D. M. 1994, ApJS, 91, 713

Menten, K. M., Pillai, T., & Wyrowski, F. 2005, in IAU Symposium, Vol. 227, Massive Star Birth: A Crossroads of Astrophysics, ed. R. Cesaroni, M. Felli, E. Churchwell, & M. Walmsley, 23

Mezger, P. G., & Henderson, A. P. 1967, ApJ, 147, 471

Momjian, E. 2017, VLA Observational Status Summary 2021A (Draft Version), Chapter 3.1: Resolution, https://science.nrao.edu/facilities/vla/docs/manuals/oss/referencemanual-all-pages

Motte, F., Bontemps, S., & Louvet, F. 2018, ARA&A, 56, 41

Müller, H. S. P., Schlöder, F., Stutzki, J., & Winnewisser, G. 2005, Journal of Molecular Structure, 742, 215

Myers, P. C., Mardones, D., Tafalla, M., Williams, J. P., & Wilner, D. J. 1996, ApJL, 465, L133

Osterbrock, D. E., & Ferland, G. J. 2006, Astrophysics of gaseous nebulae and active galactic nuclei (University Science Books)

Panagia, N. 1973, AJ, 78, 929

Peters, T., Banerjee, R., Klessen, R. S., et al. 2010a, ApJ, 711, 1017

Peters, T., Longmore, S. N., & Dullemond, C. P. 2012, MNRAS, 425, 2352

Peters, T., Mac Low, M.-M., Banerjee, R., Klessen, R. S., & Dullemond, C. P. 2010b, ApJ, 719, 831

Pineau des Forets, G., Roueff, E., Schilke, P., & Flower, D. R. 1993, MNRAS, 262, 915

Pineda, J. L., Goldsmith, P. F., Chapman, N., et al. 2010, The Astrophysical Journal, 721, 686

Remijan, A., Biggs, A., Cortes, P. A., et al. 2019, ALMA Cycle 7 Technical Handbook (NRAO)

Rosero, V., Hofner, P., Claussen, M., et al. 2016, ApJS, 227, 25

Sánchez-Monge, Á., Pandian, J. D., & Kurtz, S. 2011, ApJL, 739, L9

Saral, G., Hora, J. L., Audard, M., et al. 2017, ApJ, 839, 108

Sato, M., Reid, M. J., Brunthaler, A., & Menten, K. M. 2010, ApJ, 720, 1055

Scott, P. F. 1978, Monthly Notices of the Royal Astronomical Society, 183, 435

Sewilo, M., Churchwell, E., Kurtz, S., Goss, W. M., & Hofner, P. 2004, ApJ, 605, 285

Shi, H., Zhao, J.-H., & Han, J. L. 2010a, ApJL, 718, L181

—. 2010b, ApJ, 710, 843

Shu, F. H. 1977, ApJ, 214, 488

Shu, F. H., Adams, F. C., & Lizano, S. 1987, ARA&A, 25, 23

Tanaka, K. E. I., Tan, J. C., & Zhang, Y. 2016, ApJ, 818, 52

Thompson, M. A., & White, G. J. 2004, A&A, 419, 599

Townsley, L. K., Broos, P. S., Garmire, G. P., et al. 2014, ApJS, 213, 1

Urquhart, J. S., Figura, C. C., Moore, T. J. T., et al. 2014, MNRAS, 437, 1791

van der Tak, F. F. S., & Menten, K. M. 2005, A&A, 437, 947

Velusamy, T., Peng, R., Li, D., Goldsmith, P. F., & Langer, W. D. 2008, ApJL, 688, L87

Westerhout, G. 1958, BAN, 14, 215

Wilson, T. L., Rohlfs, K., & Hüttemeister, S. 2009, Tools of Radio Astronomy (Springer-Verlag)

Wood, D. O. S., & Churchwell, E. 1989, ApJS, 69, 831

Xu, Y., Reid, M. J., Menten, K. M., et al. 2009, ApJ, 693, 413

Yang, A. Y., Thompson, M. A., Tian, W. W., et al. 2019, MNRAS, 482, 2681

Young, L. M., Keto, E., & Ho, P. T. P. 1998, ApJ, 507, 270

Zhang, Q., & Ho, P. T. P. 1997, ApJ, 488, 241

Zhang, Q., Ho, P. T. P., & Ohashi, N. 1998, ApJ, 494, 636

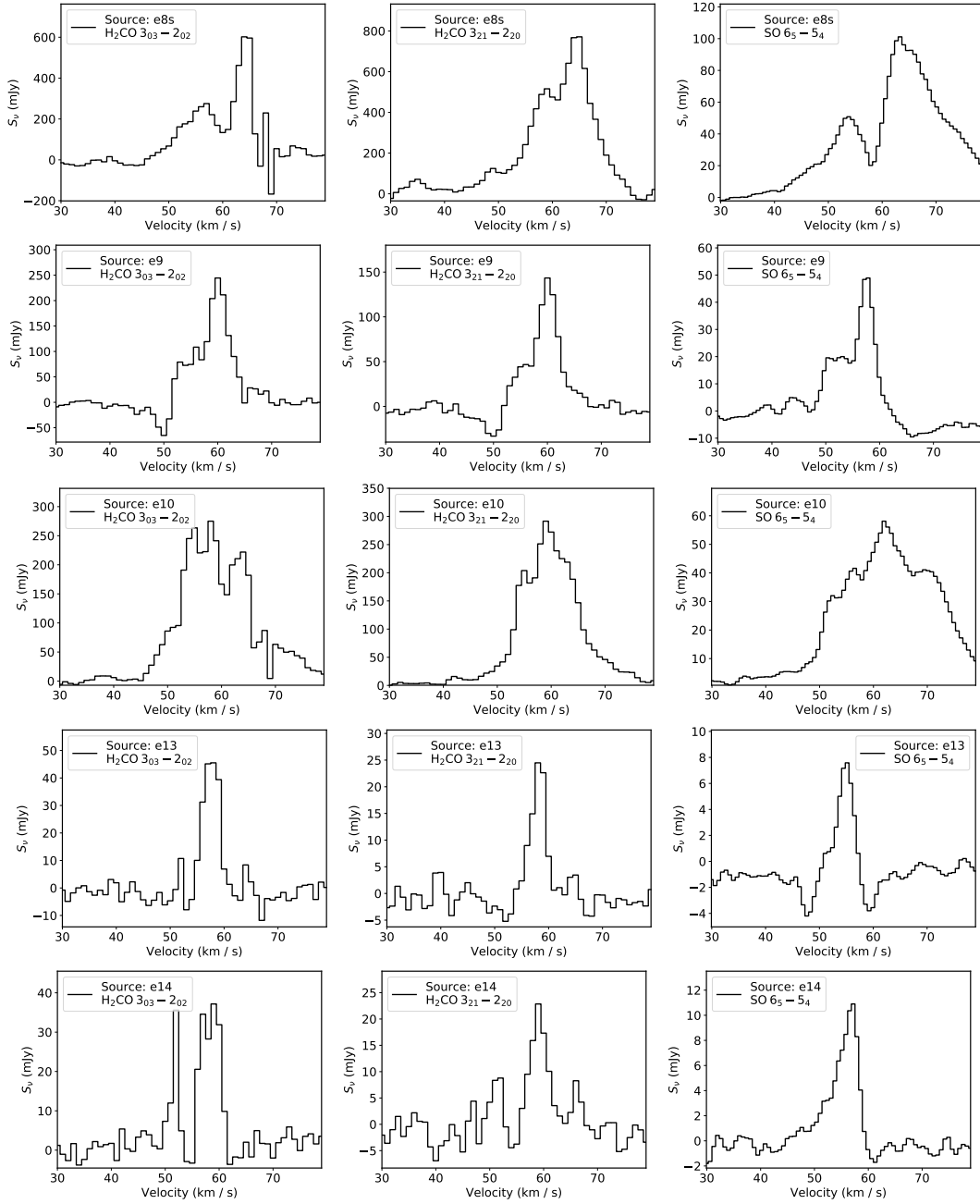Zhang, Y., Tan, J. C., Tanaka, K. E. I., et al. 2019, Nature Astronomy, 224

Figure 13. Spectral profiles of the molecular transitions $H_2CO(3_{0,3} - 2_{0,2})$ – left –, $H_2CO(3_{2,1} - 2_{2,0})$ – middle –, $SO(6_5 - 5_4)$ – right – for sources in catalog B considered in our classification of line profiles and without $H30\alpha$ detection.
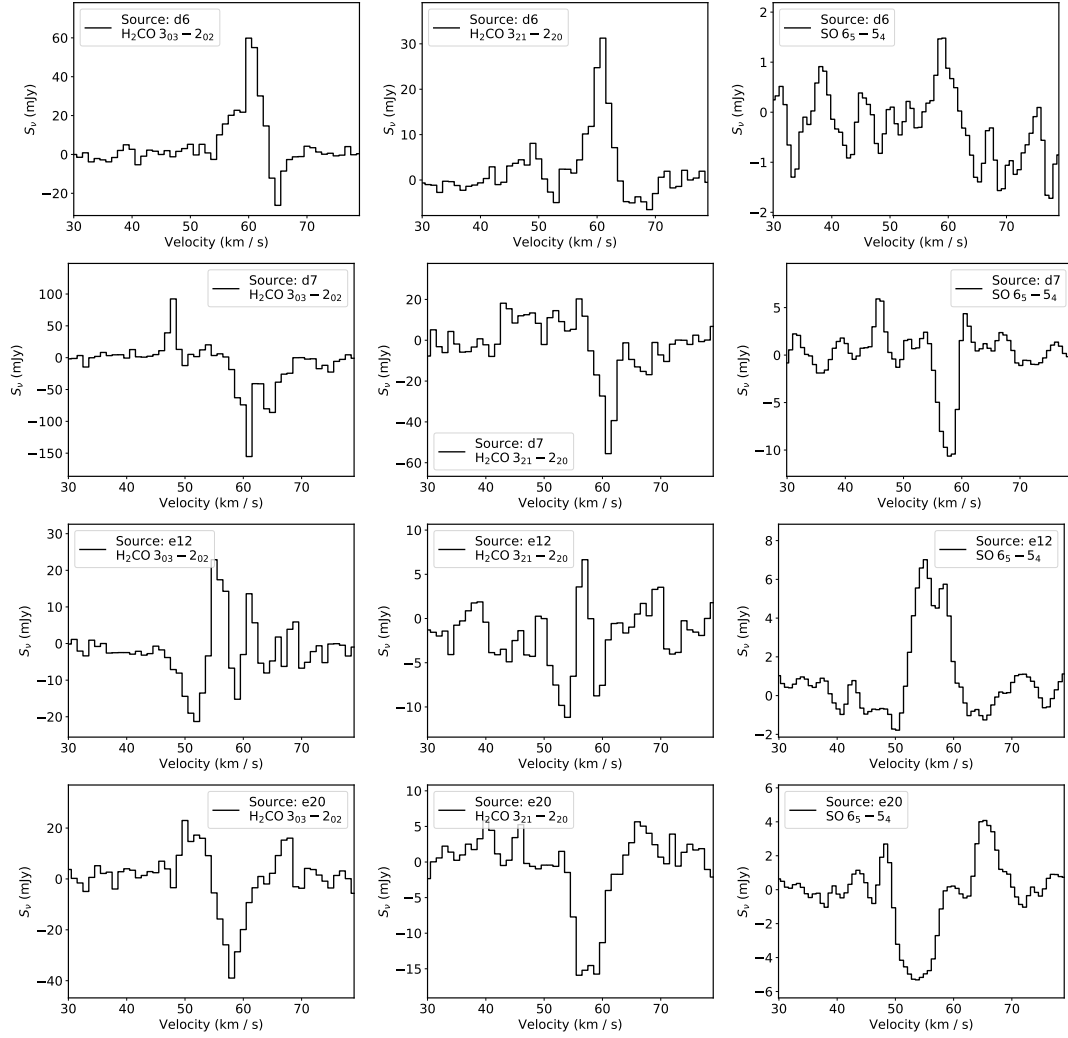
Figure 14. Spectral profiles of the molecular transitions $H_2CO(3_{0,3} - 2_{0,2})$ – left –, $H_2CO(3_{2,1} - 2_{2,0})$ – middle –, $SO(6_5 - 5_4)$ – right – for sources in catalog B which are not considered in our classification of line profiles because they are significantly affected by negative sidelobes from the brightest emission in the maps.
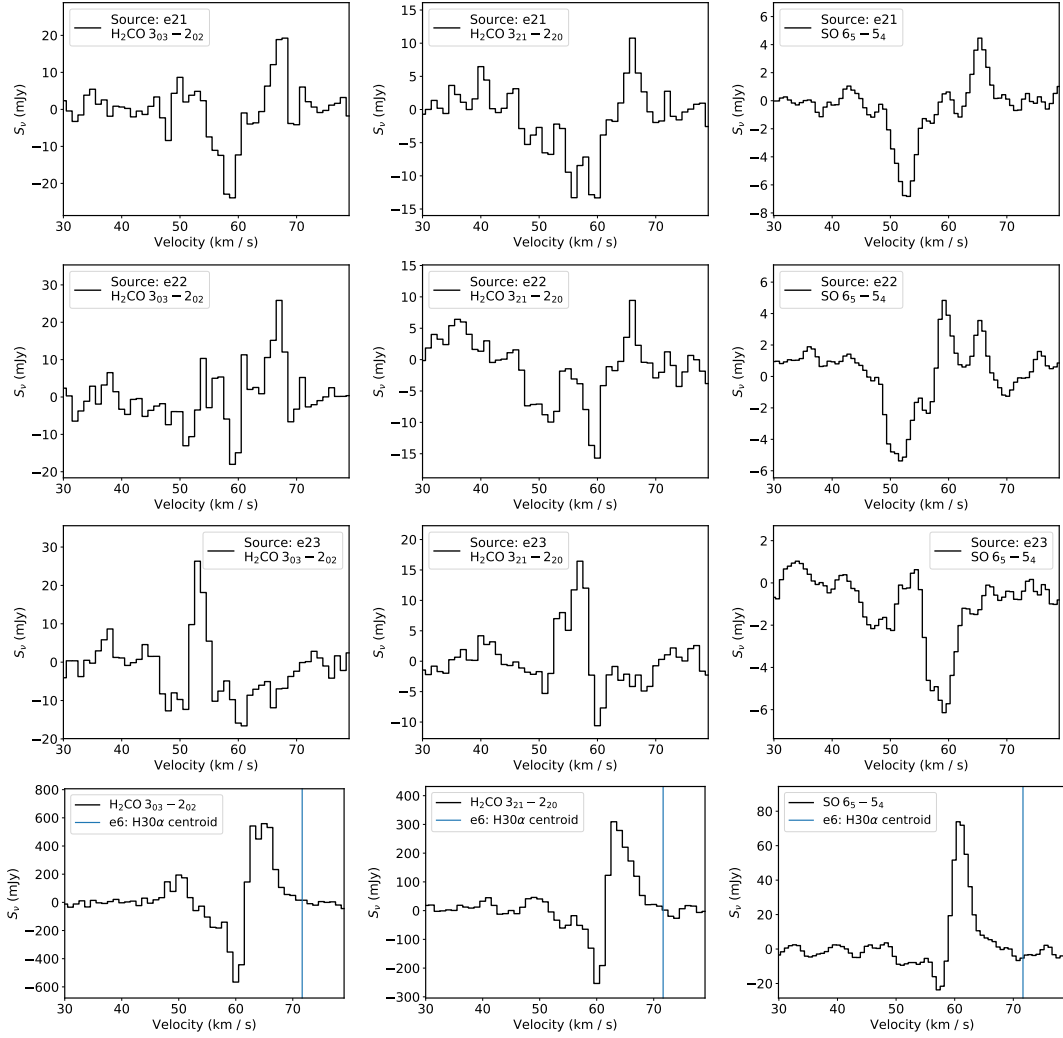
Figure 14. *contd.* Spectral profiles of the molecular transitions $H_2CO(3_{0,3} - 2_{0,2})$ – left –, $H_2CO(3_{2,1} - 2_{2,0})$ – middle –, $SO(6_5 - 5_4)$ – right – for sources in catalog B which are not considered in our classification of line profiles because they are significantly affected by negative sidelobes from the brightest emission in the maps.